Photoemission studies on Ga containing alloys in the context of SCALMS catalysis

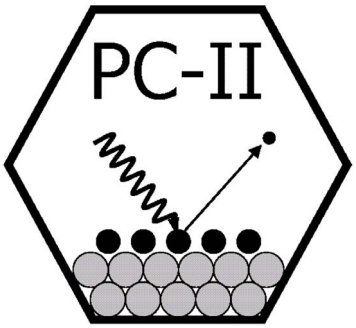

Der Naturwissenschaftlichen Fakultät der
Friedrich-Alexander Universtität Erlangen-Nürnberg
zur Erlangung des Doktorgrades Dr. rer. nat.

vorgelegt von

Haiko Wittkämper
aus Holzminden

Als Dissertation genehmigt von der Naturwissenschaftlichen Fakultät der Friedrich-Alexander-Universität Erlangen-Nürnberg

Tag der mündlichen Prüfung:	15.11.2022
Gutachter:	PD Dr. Christian Papp
	Prof. Dr. Jörg Libuda

Contents

1 Introduction

Chemical industry has a high demand for propene as the basic building block for polypropylene and several other important chemicals.[1] Most of the yearly production of propene comes from steam cracking and fluid catalytic cracking (FCC). These large-scale processes produce a variety of light hydrocarbons and can lag selectivity towards propene, depending on the reaction conditions.[2] An increasing global demand for propene results in selective processes like the dehydrogenation of propane becoming more and more important.[2]

Hence the direct dehydrogenation of propane (C_3H_8) to propene (C_3H_6) is highly desirable. It yields hydrogen and propene, two very valuable products.[3]

$$C_3H_8 \quad \rightleftharpoons \quad C_3H_6 \quad + \quad H_2 \qquad \left(\Delta H^{\ominus}_{298} = 124.3\,\mathrm{kJ\ mol^{-1}}\right)$$

Regarding its thermodynamics, propane dehydrogenation (PDH) is an endothermic reaction with increasing molarity, therefore, according to Le Chatelier's principle, the best conversion is expected at high temperatures, typically 550-850°C, and relatively low pressures, typically around 1-2 bar. Unfortunately, the reaction energetics of the C-H bond cleavage in the PDH reaction are similar to those of the C-C bond cleavage, which leads to the cracking of propane to ethylene (C_2H_4) and methane (CH_4), which is similarly endothermic. To achieve a high propene yield in an on-purpose PDH process, it is therefore of paramount importance to have high selectivity towards the propane-propene equilibrium.[1]

The industrial standard catalysts are Pt nanoparticles on an Al_2O_3 support, typically with Sn as promoter, or Cr_2O_3 nanoparticles, similarly supported on Al_2O_3. Various other oxides such as VO_3, MnO_2 and notably also Ga_2O_3 show catalytic activity as well.[4] As for all catalytic processes that involve short hydrocarbons at high-temperatures, significant attention needs to be paid to coke formation. The polycondensation of reaction intermediates to a mostly graphitic deposit (coke) that covers/blocks the active sites of the catalysts and clogs pores in porous support materials, is considered the main deactivation route for PDH catalysts. Coke formation is combated by regular regeneration steps, in

which an oxygen-rich feed is provided to burn off coke deposits.[5, 6, 7] In technical applications, this is realized by either cycling several reactors between dehydrogenation, regeneration and purging steps (CATOFIN process) or by using a fluidized bed, which allows for continuously moving the catalyst through different reactors and regeneration units (OLIFLEX process). Typical on-stream times in these processes are on the order of a few minutes (20 min and below). A notable exception is the Uhde STAR process, where a PtSn on Zn-doped Al_2O_3 catalyst is used, and on-stream times of up to 6 h are reached.[1, 4]

Due to the economically desirable products and the ecologically favorable reduction of waste products, an ongoing search for catalysts that allow for longer on-stream times while simultaneously maintaining high activities and selectivities is going on. In 2017, Taccardi et al. introduced supported GaPd alloys with low Pd content as very active, selective and stable PDH catalysts, which, without extensive optimization, outperform the industrial standard catalysts.[8] The material was designed according to a catalytic concept pioneered at FAU Erlangen-Nürnberg that is referred to as supported catalytically active liquid metal solutions (SCALMS).[9] This performance underlines the potential of SCALMS, since pure Pd is not well suited as a dehydrogenation catalyst due to excessive coke formation.

The current working hypothesis for SCALMS is that a Ga-transition metal alloy, which is liquid under reaction conditions, is the active phase of these catalysts. In this liquid alloy, Ga is considered as an inert matrix material, in which the active component is dispersed atomically and therefore provides highly uniform, isolated reaction sites at the liquid metal/gas interface.

PDH, and dehydrogenation reactions in general, are considered to be highly site-specific reactions. Biloen et al. reported 1976 that in a dilution series of AuPt alloys from 14 to 0.5 at.% Pt in Au, the reaction rate of PDH decreased linearly with the Pt content.[10] Such kinetic experiments, in which the reaction rate is evaluated along a dilution series of a catalytically active metal (Pt) diluted by an inactive metal (Au), allow for assessing the influence of the ensemble size, meaning the number of active metal atoms involved in the rate-determining step of the reaction.[11] Biloen et al. concluded that no specific ensemble size is especially favorable for the PDH reaction and that, in principle, single Pt atoms should be able to catalyze the reaction.[10] Especially for costly elements like Pt, Pd and Rh, a single-atom catalyst is highly desirable since the transition metal is used with ultimate efficiency. Furthermore, interesting catalytic properties, especially high

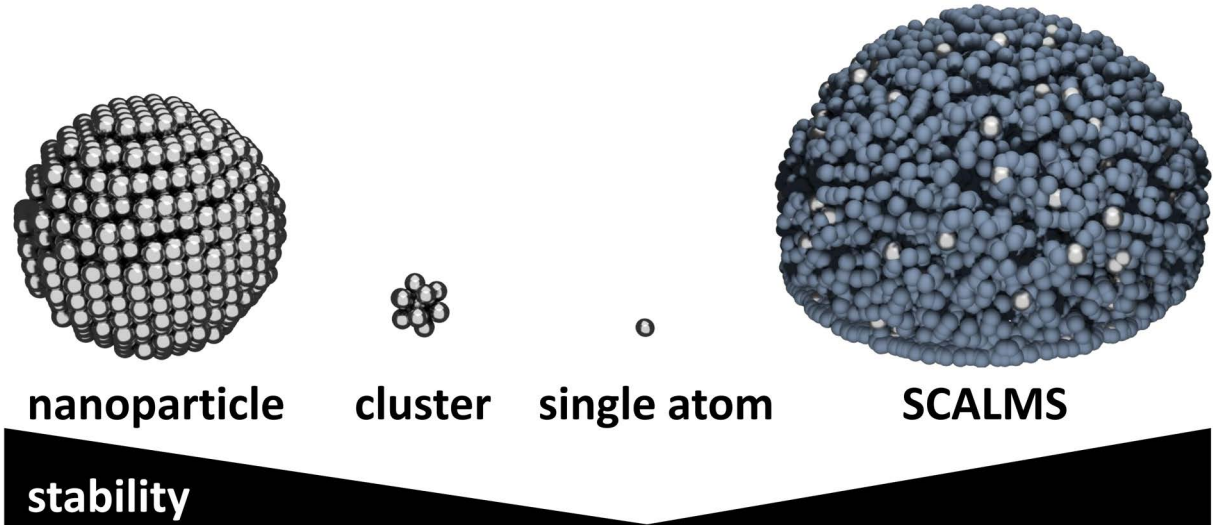

Figure 1 Schematic illustration of the stability relationships between (larger) nanoparticles, clusters, single atoms and SCALMS. With decreasing particles size, the number of under-coordinated atoms increases, what results in decreasing stability. In the liquid SCALMS alloy, on the other hand, the dispersed single transition metal atoms are stabilized by the neighboring Ga atoms.

selectivity, are to be expected. The main challenge in designing such catalysts is to provide stable single-atom reactive centers under reaction conditions. In recent years, single-atom catalysis (SAC) has developed into an independent field of research dedicated to the development and investigation of such catalysts.[12, 13, 14, 15] Several ways to achieve the stabilization of single-atom sites, e.g., by utilizing the interplay between catalytically active single transition metal atoms and specific, stabilizing positions on oxidic support particles[16], by confining single atoms into the pores of a zeolites[17], or by incorporating catalytically active atoms in an inactive matrix as a disordered substitutional alloy (single-atom alloy catalysis)[12] have been reported. Additionally, in some cases, intermetallic phases can provide catalytically interesting, isolated metals sites at their surfaces due to their crystal structures. Within the field of SAC, SCALMS falls into the category of substitutional alloys.

Another, closely related parameter that may be used to optimize the active sites of a catalyst is site uniformity. In typical heterogeneous catalysis, the variance in active sites is high. Nanoparticles and clusters typically provide several different crystal facets, edges and corners, all of which present sites with varying activity that may favor different reaction products. Additionally, defect sites and the interface between the active metal and the support increase the number of different catalytically active atom constellations

even more. For classical heterogeneous catalysis, the control over such irregularities is very limited.[18] In liquid metals, however, the catalyzed reaction occurs at the liquid metal to gas interface. These interfaces are, in contrast to the for heterogeneous catalysis typical nanoparticles, generally considered as very well defined and mostly defect free due to the interplay of the high mobility and the surface tension of the liquid.[19, 20] For catalysis, such interfaces present highly uniform reaction sites, thereby, allowing for a degree of active site control that is usually reserved for homogeneous catalysis. Besides SCALMS, other liquid metal catalysts have shown outstanding results, underlining the potential of these materials.[21, 22, 23]

A third peculiarity of SCALMS systems is the dynamics at the liquid metal/gas interface. Due to the neglectable solubility of hydrocarbons in liquid Ga, the reaction is catalyzed exclusively at the liquid metal/gas interface. All spectroscopic and computational findings, however, suggest that the liquid metal surfaces of GaPd[8, 24], GaPt[25] and GaRh[26], the so far investigated SCALMS systems, are depleted of the active components. This led to the proposal of dynamically formed active sites. According to this mechanism, for the dehydrogenation reaction to occur, single transition metal atoms move to the otherwise transition metal-depleted surface and catalyze the reaction.[8, 24, 26, 27, 28, 29, 30] Operando infrared spectroscopy combined with molecular dynamics (MD) calculations support that for liquid GaPt alloys such dynamically appearing Pt atoms at the otherwise Pt-depleted Ga surfaces may exist under reaction conditions.[31]

From the beginning, x-ray photoemission spectroscopy (XPS) played a crucial role in developing an atomic scale understanding of SCALMS catalysis.[8, 25, 32] Often, real catalysts are not accessible to XPS due to the high material complexity and the fact that XPS relies, at least partly, on high vacuum techniques. In literature, these challenges are, in a more general context regarding Surface Science and applied catalysis, referred to as the materials and pressure gap.[33, 34] XPS and other surface science techniques have, however, been successfully applied to technically relevant materials. One way of doing so is by choosing well-fitting but greatly simplified model systems, and extrapolating information from these to the real material. The information flow is schematically illustrated in Figure 2. A similar approach was applied by Grabau et al. who conducted XPS studies on macroscopic droplets of liquid, binary, GaPd, GaPt and GaRh alloys as model systems for the catalytically active phase of SCALMS catalysts.[8, 24, 25, 26] These model systems allowed for avoiding the influence, undefined nature and complex geometry of the support materials. XPS studies show a temperature-dependent

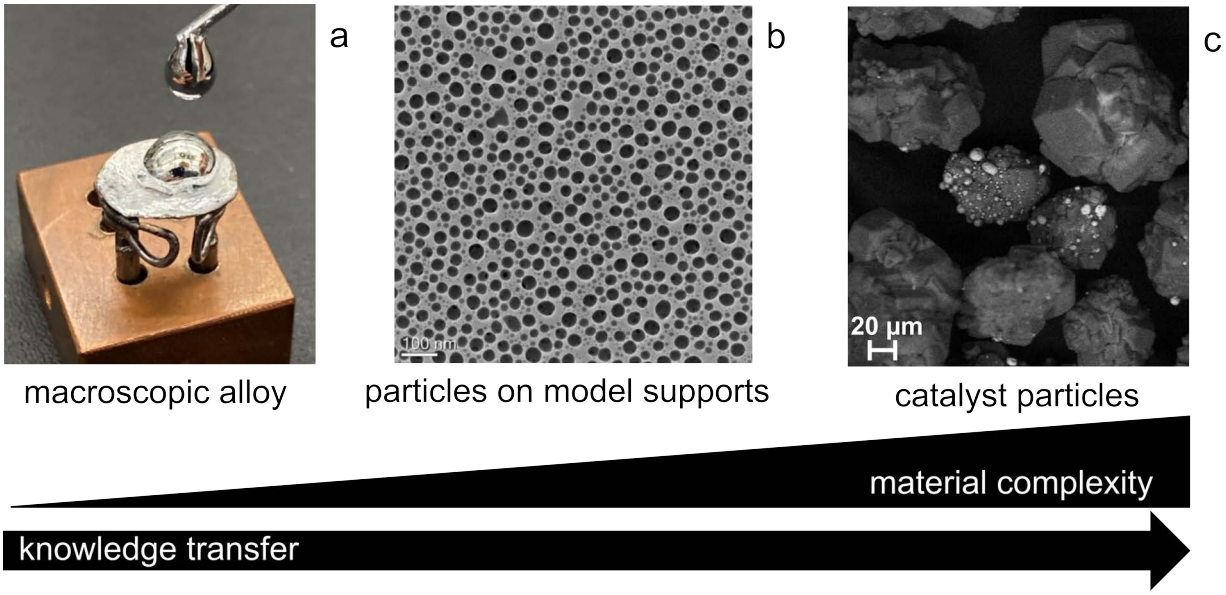

Figure 2 Schematic illustration on the bridging of the material complexity gap in the context of SCALMS catalysis. Information is inferred from (a) macroscopic binary alloy droplets to (b) metal particles on flat model supports, here shown by transmission electron microscopy, to (c) real SCALMS particles, here shown by scanning electron microscopy. ((a) Adapted and modified from [35], copyright 2021 with permission by Elsevier.)

Pd, Pt and Rh surface concentration that is linked to the precipitation of transition metal-rich GaPd, GaPt and GaRh intermetallic phases in the bulk of the macroscopic liquid metal droplets.[8, 24, 25, 26] The found phase transitions were additionally supported by *in situ* heating transmission electron microscopy (TEM) and electron diffraction.[26, 36] A second important result is a layering along the alloy-to-vacuum interface with a transition metal depletion of the first atomic layer and the second atomic layer being transition metal-enriched. This was observed by simultaneously recording bulk-sensitive (normal emission) and surface-sensitive (80° emission angle) XP spectra of liquid GaPd and GaRh alloys. *Ab initio* MD studies reproduce these findings.[8, 24, 25] The observed transition metal depletion of the alloy surface led to the proposed dynamic mechanism for SCALMS, that was outlined in the last section.

This cumulative thesis comprises the authors contributions to six publications presenting photoemission studies on macroscopic GaRh and GaPd alloys, GaRh and GaPt particles systems, macroscopic GaIn alloys, and GaRh intermetallic phases. All results were presented and interpreted in the broader context of SCALMS catalysis. Before recapitulating the obtained results in Chapter 4, the following two chapters will pro-

vide the reader with an introduction to the qualitative and quantitative interpretation of photoemission spectra (Chapter 2), and an overview to the used instruments and materials (Chapter 3). In Chapter 4.2 near-ambient pressure oxidation studies of macroscopic GaRh and GaPd alloys are presented. These build on previously reported XPS studies on the incorporation of Pt in Ga_2O_3 observed *in situ*, during the oxidation of GaPt alloys.[32] There, Chapter 4.3 continues to results on more complex model systems, meaning GaPt and GaRh metal particles prepared by physical vapor deposition on flat model supports, investigated with synchroton XPS. It is found that the results obtained from macroscopic GaRh alloys are transferable to GaRh particles on flat SiO_2/Si supports. Chapter 4.4 presents studies on the synthesis and synchrotron XPS surface characterization of two catalytically highly interesting GaRh intermetallic phases, Ga_9Rh_2 and Ga_3Rh. The research on GaRh SCALMS is naturally intertwined with the research on GaRh intermetallic phases.[26, 36] Both Ga_9Rh_2 and Ga_3Rh present important reference materials for GaRh SCALMS and are, based on what is known for the propane dehydrogenation reaction, highly interesting as potentials catalysts. Chapter 4.5 describes temperature-dependent XPS studies on binary alloys of two p-block metals, Gallium and Indium. A temperature-dependent surface enrichment of In is found. This result is highly relevant as first step towards ternary alloy SCALMS catalysts, for which low melting GaIn alloys are considered as a potential inactive matrix material. As a conclusion to this thesis, Chapter 5 gives a summary of the presented results.

2 Fundamentals

This thesis presents synchrotron- and lab-based photoemission studies of catalytically highly interesting Ga alloy systems and Ga intermetallic phases. As a foundation for the presented results, this Chapter will provide background on the basics of photoemission spectroscopy, namely the qualitative interpretation of XP spectra, quantitative XPS and the photoemission cross sections that are necessary to conduct these investigations.

2.1 Photoemission and photoemission spectroscopy

When materials are irradiated with light such as UV light or X-rays, the emission of electrons is observed. This is referred to as the photoelectric effect and was initially described by Hertz (1887).[37] The correct interpretation was given by Einstein in 1905[38] and was awarded the Nobel Price in physics (1921)[39]. Continuing progress in vacuum technology and the availability of electron/ion optical elements, allowed for the development of spectroscopic techniques based on the photoelectric effect in the 50s to 60s of the 20th century.[40, 41] Today, photoelectron spectroscopy is routinely used for the qualitative and quantitative chemical analysis of material surfaces, in fields ranging from fundamental research to applied semiconductor electronics and applied catalysis.

2.2 XP spectrum, binding energy and chemical shift

The underlying concept of photoemission spectroscopy is energy conversion: Electrons in atoms are bound at specific binding energies corresponding to their atomic orbitals. Upon irradiation, an electron may absorb a photon; thereby, the energy of the photon is transferred to the electron, which is emitted from the atom, provided the photon energy is high enough. In Equations, the kinetic energy (E_{kin}) of a photoelectron emitted from a material, where it is bound at binding energy (E_{b}), is given as

$$E_{\mathrm{kin}} = \mathrm{h}\nu - E_{\mathrm{b}} - \phi_{\mathrm{sample}}, \tag{1}$$

where $h\nu$ is the energy of the exciting photon and ϕ_{sample} is the work function of the sample, meaning the energetic difference between the Fermi energy and the vacuum energy level.[42] Figure 3a illustrates an energy level diagram for the excitation of a photoelectron out of the topmost L shell (L_3, $2p_{3/2}$ orbital), for a fourth row p-block element such as Ga ([Ar] $3d^{10}4s^24p^1$). A second effect that commonly results in prominent

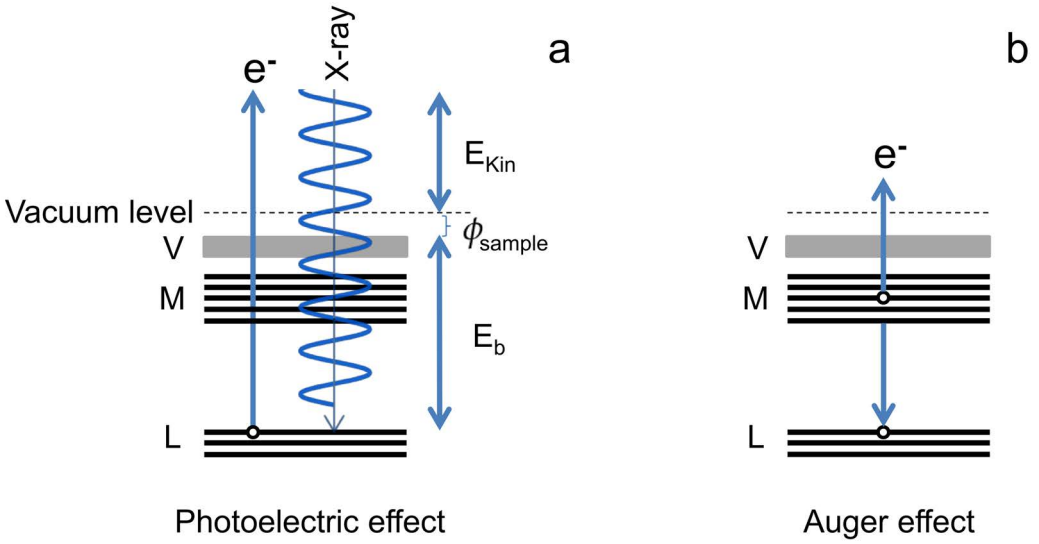

Figure 3 Energy diagram of (a) the photoelectric effect and (b) the Auger effect. Shown are the L, M and valence (V) shells of a fourth row p-block element such as Ga.

emission lines recorded in X-ray photoemission spectra is the Auger effect. The Auger effect is a radiation-less decay of "core holes" under the emission of an electron from a weaker bound state. Figure 3b illustrates a $L_3M_1M_3$ Auger transition, in which a core hole in the L_3 shell ($2p_{3/2}$ state) is filled by an electron from the energetically higher laying M_1 shell ($3s_{1/2}$ state) and the gained energy being transferred to an electron in the M_3 shell ($3p_{3/2}$ state), which is in turn emitted from the material.

Since electrons are charged particles and, therefore, strongly interact with matter, they quickly lose their kinetic energy due to inelastic scattering. For this reason, only photoelectrons generated at the surface and in the surface-near region of a sample leave the material and contribute to the generated photocurrent. To generate a spectrum, the photoelectrons emitted from an irradiated sample are selected according to their kinetic energy using a dispersive, electron-optical element, before detecting the spectrum as an energy-dependent photocurrent. The recorded spectrum is commonly shown as intensity, meaning detector counts ($\propto$ photocurrent) against binding energy, calculated from Equation 1. An exemplary photoemission spectrum recorded of a liquid elemental

Ga sample excited using a non-monochromatized x-ray tube with an aluminium anode (Al Kα radiation, h$\nu_{\mathrm{Al\,K}\alpha}$= 1486.6 eV)[43] is shown in Figure 4a. In the spectrum, parts of the L shell ($2p_{1/2}$, $2p_{3/2}$ states), multiple LMM Auger lines and the M shell (3s, 3p and 3d states) are visible.

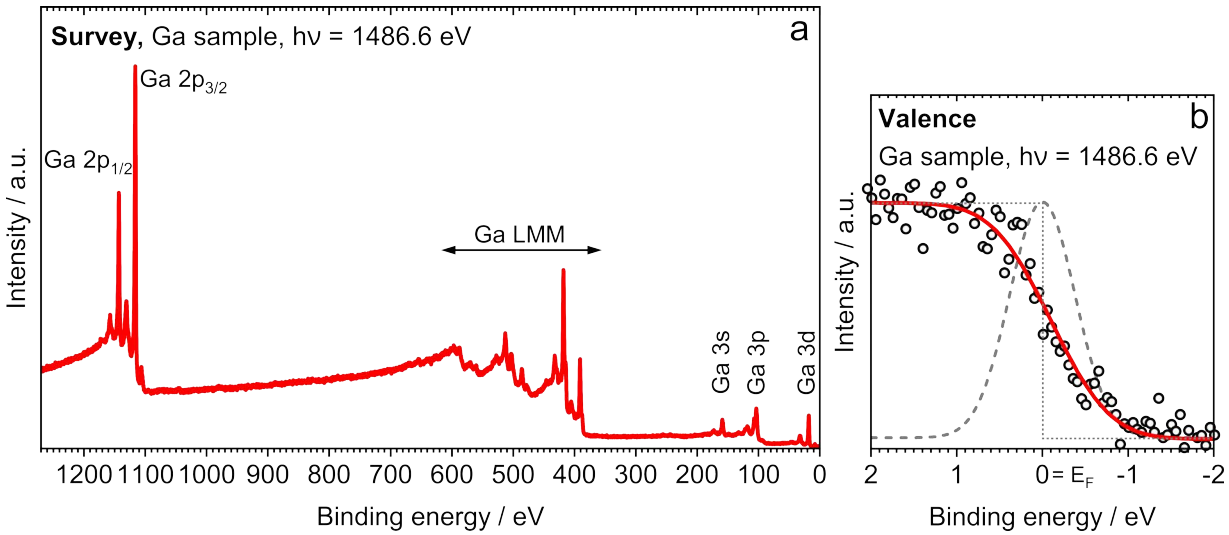

Figure 4 (a) Survey spectrum of elemental Ga and (b) valence band edge of elemental Ga, fitted using Equation 2 and used for binding energy referencing. In addition, the step function Θ and the Gaussian it was convoluted with to obtain the fit function are shown.

To make spectra measured on different machines comparable, accurate calibration of the binding energy scale to a common point is necessary. For metallic samples, one possibility is to use the valence band edge as a common zero-point of the binding energy scale, Figure 4b.

In most metals, the shape of the valence band edge is dictated by the Fermi-Dirac distribution $f_{\mathrm{FD}}(E_{\mathrm{b}}; T, \mu_{\mathrm{e}} \approx E_{\mathrm{F}})$ due to the nature of electrons as fermions.[44, 45] This distribution contains the temperature T and the chemical potential of the electron μ_{e}, approximated as Fermi energy E_{F}, as parameters. It models the temperature-dependent excitation of electrons into unoccupied states, this effect is, however, relatively small, the width of the distribution is approximately $4k_{\mathrm{B}}T$ (0.1 eV for 300 K)[46], and is therefore often times practically approximated as a 0 to 1 step function $\Theta(E_{\mathrm{b}})$):

$$f_{\mathrm{FD}}(E_{\mathrm{b}}; T, E_{\mathrm{F}}) = \frac{1}{\exp\left(\frac{-(E_{\mathrm{b}}-E_{\mathrm{F}})}{k_{\mathrm{B}}T}\right)+1} \underset{\text{(for XPS)}}{\approx} \Theta(E_{\mathrm{b}}-E_{\mathrm{F}}) = \begin{cases} 0: & E_{\mathrm{b}}-E_{\mathrm{F}} < 0 \\ 1: & E_{\mathrm{b}}-E_{\mathrm{F}} \geq 0 \end{cases}.$$

Notable exceptions from this approximation are very high-resolution experiments.[45] In addition to the occupation, the instrumental broadening needs to be taken into account to reproduce the shape of a measured valence band edge.[45, 46] This is done by convoluting[47] the step function $\Theta(E_\mathrm{b} - E_\mathrm{F})$ with a Gaussian $g(\tau)$ that resembles the spectroscopic broadening:

$$\begin{aligned}(g * \Theta)\,(E_\mathrm{b} - E_\mathrm{F}) &= \int_{-\infty}^{\infty} g(\tau) \cdot \Theta(E_\mathrm{b} - E_\mathrm{F} - \tau)\,\mathrm{d}\tau \\ &= \int_{-\infty}^{E_\mathrm{b}-E_\mathrm{F}} \frac{1}{a\sqrt{\pi}} \exp\left(-\frac{\tau^2}{a^2}\right) \mathrm{d}\tau \\ &= \frac{1}{2}\left(1 + \mathrm{erf}\left(\frac{E_\mathrm{b} - E_\mathrm{F}}{a}\right)\right), \end{aligned} \tag{2}$$

where erf is the Gauss error function and a is a parameter related to the full width at half maximum (FWHM) of the Gaussian. Figure 4b shows the measured valence band edge of liquid Ga sample, fitted with Equation 2. Based on the fit, the binding energy is corrected by choosing E_F as the zero point of the binding energy scale. In addition, for fits obtained from the valence band edges of well defined reference samples with neglectable Gaussian contributions from the sample, the FWHM calculated from the parameter a, $\mathrm{FWHM} = 2\sqrt{\ln(2)}a$, is commonly used as a measure for the spectroscopic resolution.

XP spectra with a careful binding energy correction and good spectroscopic resolution can often times provide extensive details on the chemical state of the detected elements. Figure 5 shows a high resolution region scan for the Ga 3d core level of a pure Ga sample in (a) and a slightly oxidized Ga sample in (b). While the purely metallic sample (a) shows a spin-orbit-split doublet with the Ga $3d_{5/2}$ component at 18.4 eV, as is expected for metallic Ga, the sample with Ga suboxide (b) shows additional components (orange lines) shifted to higher binding energies (20 eV for the $3d_{5/2}$ component). Such binding energy differences are referred to as chemical shifts, because they contain information on the chemical state of the detected atoms. In the example shown in Figure 5b, a shift of 1.6 eV to higher binding energy suggests the formation of a sub-stoichiometric Ga oxide Ga_2O. For the components of fully oxidized Ga_2O_3, seen in (c) (red lines), larger shifts of around 2.0-2.4 eV to higher binding energies are observed.[48] Intuitively, the chemical shifts can be interpreted as the core level electrons reacting to the chemical environment of the atom. In case of the given example, the chemical shifts in Ga_2O can be viewed as electronegative O atoms pulling away electron density from Ga, which results in the

remaining electrons being more strongly bound to the nucleus and therefore showing higher binding energies in their XP spectra.

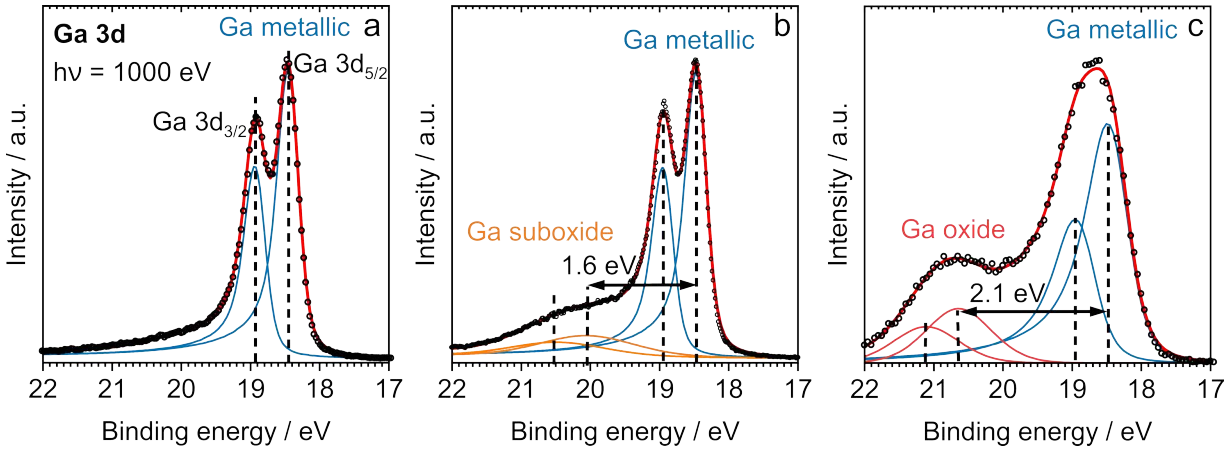

Figure 5 High-resolution XP spectra of the Ga 3d region for (a) a metallic Ga sample, (b) a Ga sample with Ga suboxide on the surface and (c) a Ga sample were the surface is fully oxidized to Ga_2O_3.

While oftentimes very successful, an interpretation of observed core level shifts purely based on chemical reasoning can be misleading. For a more complete picture of core level shifts observed in XP spectra, it is convenient to view the observed binding energy E_b as the difference between the total energy of an N-particle state before photoionization, the initial-state energy $E_{in}^{total}(N)$, and the total energy of the photoionized (N-1) particle state, the final-state energy $E_{fin}^{total}(N-1)$:

$$E_b = E_{fin}^{total}(N-1) - E_{in}^{total}(N), \tag{3}$$

notice the sign convention, in electronic structure theory $E_{in}^{total}(N)$ and $E_{fin}^{total}(N-1)$ typically have a negative sign, while E_b in photoemission spectroscopy is typically positive. In the purely chemical picture, the final-state energy is approximated as the initial-state energy minus the orbital energy of the electron removed in the photo excitation process. This approximation is referred to as Koopmans-Theorem. It ignores that all the other (N-1) electrons will react to the removal of the N-th electron, and "relax" into more favorable spatial distributions. A more correct final-state energy is therefore given as

$$E_{fin}^{total}(N-1) = E_{fin}^{total}(N-1)^{KT} + \delta_{relaxation}, \tag{4}$$

where the superscript *KT* indicates Koopmans-Theorem. A reliable interpretation of XP binding energies requires that both, effects that influence $E_{\text{fin}}^{\text{total}}(N-1)$, final-state effects, and effects that influence $E_{\text{in}}^{\text{total}}(N)$, initial-state effects, are taken into account.[42]

In the context of this thesis, such final state effects are relevant for the interpretation of the Rh 3d and Pd 3d binding energies of GaRh/GaPd intermetallic phases and macroscopic GaPd alloys. For these materials, the electronegativity difference between Ga, Rh and Pd (Pauling Scale: Ga 1.6, Rh 2.2 and Pd 2.2)[49] suggests negative charge transfer from Ga to Rh/Pd, which is also reproduced in DFT calculations. Therefore, in a pure initial-state picture of the XPS binding energy, a core level shift to lower binding energy compared to the pure elements is expected. However, experimentally, shifts to higher binding energy are observed. DFT calculations reveal that this is due to significantly different relaxations around the formed core holes (different $\delta_{\text{relaxation}}$) for these materials compared to pure Rh and Pd. Additional details are given in corresponding Chapters 4.2, 4.3 and 4.4 as well as in the publications.[50, 51]

2.3 Quantitative XPS

A strength of photoemission spectroscopy, besides the qualitative interpretation of binding energies, is that the technique is inherently quantitative. Intensities, meaning peak areas in a measured XP spectrum, are linked to the sample surface-composition. An extensive discussion is presented by Seah et al. e.g. in [52] and [53]. Herein, the total photo current I_A originating from the photoionization of a core level A, practically given as the integrated signal area of a XPS signal, is discussed as

$$I_\mathrm{A} = \int_0^\infty \sigma_\mathrm{A} T_\mathrm{A}^\mathrm{inst.} J_{\mathrm{h}\nu} n_\mathrm{A}(z) \exp\left(-\frac{z}{\lambda_\mathrm{A}(z)\cos(\gamma)}\right) \mathrm{d}z. \tag{5}$$

In this Equation, σ_A is the total photoemission cross section of core level A, $T_\mathrm{A}^\mathrm{inst.}$ is an instrumental factor, $J_{\mathrm{h}\nu}$ is the photon flux from the excitation source and $n_\mathrm{A}(z)$ is the density of atoms A along the sample normal. The exponential dampening factor contains the inelastic mean free path (IMFP) $\lambda_\mathrm{A}(z)$ of the photoelectron from the core level A in the investigated material, and along the angle γ between the sample normal and the detector. The expression is integrated along the sample normal starting at the surface ($z = 0$) and ending at infinite depth in the bulk. In the measurements presented the angle γ is always $0°$ (normal emission), therefore the expression further simplifies ($\cos(0°) = 1$).

In case of a homogeneous sample, the composition along the surface normal is constant $n_\mathrm{A}(z) = n_\mathrm{A}$. In this case the IMFP is constant $\lambda_\mathrm{A}(z) = \lambda_\mathrm{A}$. Evaluating Equation 5 yields

$$\begin{aligned} I_\mathrm{A}^\mathrm{Hom.} &= \int_0^\infty \sigma_\mathrm{A} T_\mathrm{A}^\mathrm{inst.} J_{\mathrm{h}\nu} n_\mathrm{A} \exp\left(-\frac{z}{\lambda_\mathrm{A}}\right) \mathrm{d}z \\ &= \left[-\sigma_\mathrm{A} T_\mathrm{A}^\mathrm{inst.} J_{\mathrm{h}\nu} n_\mathrm{A} \lambda_\mathrm{A} \exp\left(-\frac{z}{\lambda_\mathrm{A}}\right)\right]_0^\infty \\ &= \sigma_\mathrm{A} T_\mathrm{A}^\mathrm{inst.} J_{\mathrm{h}\nu} n_\mathrm{A} \lambda_\mathrm{A}. \end{aligned} \tag{6}$$

Besides the estimation of XPS intensities, Equation 6 allows for a straightforward quantification of homogeneous samples. A good strategy is comparing relative peak intensities; this way a more accurate result is obtained, because common errors may cancel. Furthermore, if both intensities are measured at the same photon flux, $J_{\mathrm{h}\nu}$ eliminates from the

fraction. E.g. in case of a binary sample consisting of the elements with measurable core levels A and B, the molar fraction x_A may be estimated according to

$$x_A = \frac{n_A}{n_A + n_B} = \frac{I_A \left(\sigma_A T_A^{\text{inst.}} \lambda_A\right)^{-1}}{\left(I_A \left(\sigma_A T_A^{\text{inst.}} \lambda_A\right)^{-1}\right) + \left(I_B \left(\sigma_B T_B^{\text{inst.}} \lambda_B\right)^{-1}\right)}$$

and for more than two components accordingly.

For the results presented in thesis, besides photoemission from homogeneous samples, understanding photoemission from layered systems is highly relevant, e.g. in case of an oxide "skin" on top of a metal or a surface layer that differs from the bulk composition due to segregation effects. In such cases, the photocurrent I_A^{ol} originating for the photoionization of a core level A in a homogeneous overlayer can be estimated by integrating Equation 5 not to infinity but only up to a layer-thickness d:

$$\begin{aligned} I_A^{\text{ol}} &= \int_0^d \sigma_A T_A^{\text{inst.}} J_{h\nu} n_A^{\text{ol}} \exp\left(-\frac{z}{\lambda_A^{\text{ol}}}\right) \mathrm{d}z \\ &= \left[-\sigma_A T_A^{\text{inst.}} J_{h\nu} n_A^{\text{ol}} \lambda_A^{\text{ol}} \exp\left(-\frac{z}{\lambda_A^{\text{ol}}}\right)\right]_0^d \\ &= \sigma_A T_A^{\text{inst.}} J_{h\nu} n_A^{\text{ol}} \left(\lambda_A^{\text{ol}} - \lambda_A^{\text{ol}} \exp\left(-\frac{d}{\lambda_A^{\text{ol}}}\right)\right), \end{aligned} \tag{7}$$

where n_A^{ol} is the atom density of atoms with core level A in the overlayer and λ_A^{ol} is the IMFP of photoelectrons from core levels A within the overlayer.

For a homogeneous bulk layer below such an overlayer, Equation 6 can be modified by multiplying with an exponential dampening factor that accounts for the attenuation of the photoelectrons by the overlayer:

$$I_A^{\text{bulk}} = \sigma_A T_A^{\text{inst.}} J_{h\nu} n_A^{\text{bulk}} \lambda_A^{\text{bulk}} \exp\left(-\frac{d}{\lambda_A^{\text{ol}}}\right), \tag{8}$$

with n_A^{bulk} being the atom density in the bulk layer and λ_A^{bulk} being the IMFP of photoelectrons from core levels A within bulk layer.

Equations 6, 7 and 8 build a versatile tool set for quantitative XPS and lay at the foundation of the XPS quantifications and intensity estimations presented in the publications introduced in this thesis.

Figure 6a and b show the application of these Equations, in 6a for the intensity estimation of a homogeneous sample and in 6b for the intensity estimation of a layered sample with an oxidic overlayer.

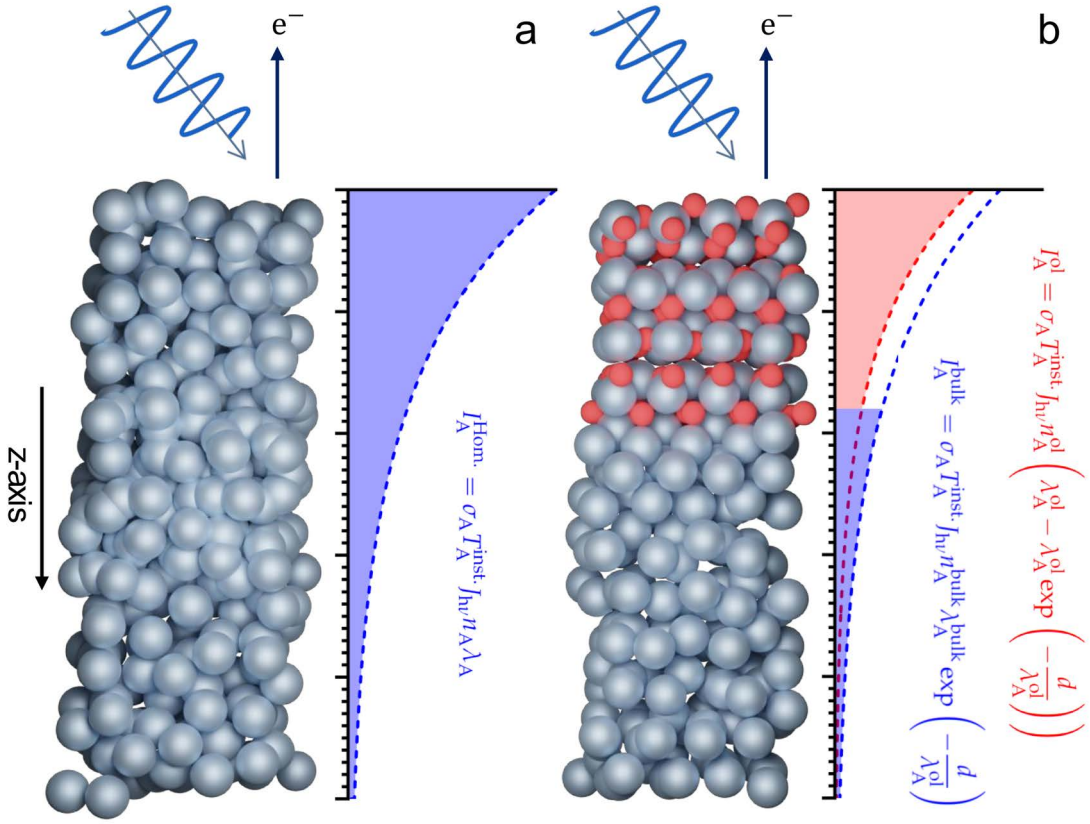

Figure 6 Visualization of the integrals leading to Equations 6, 7 and 8. In (a), the ball model represents the randomly oriented atoms in a homogeneous liquid alloy and in (b) a layered system with an oxide layer on top followed by a liquid alloy layer is shown. The integrals for the intensity estimation are color-coded in red and blue. (Atomic coordinates for the renderings were kindly provided by Sven Maisel.)

For σ, tabulated values are available for all atoms[54, 55, 56, 57] and for measurements conducted with hemispherical analyzers, $T_A^{inst.}$ is commonly approximated as close to the inverse of the kinetic energy of the detected electrons $1/E_{kin}^{A}$.[58] The IMFP of the photoelectrons can be calculated according to the TPP2M algorithm.[59] Alternatively, well-defined reference materials, for which n and λ are known, are used to express σ and T. This oftentimes results in more accurate quantification results.

2.4 Photoemission cross section and angular distribution

In the so far outlined intensity estimations, σ_A was approximated as the total photoemission cross sections, however, in some of the presented publications additional corrections accounting for asymmetries in the photoemission cross sections that depend on the experimental geometry have been employed. The derivation of the differential cross section is sketched on pages 482-483 of the Quantum Theory book by Beth[60], further details are given by Fadley[42] and Cooper[61, 62, 63]. These considerations lead to the Bethe-Cooper-Zare formula that gives the differential crossection $\frac{d\sigma_i}{d\Omega}$ for photoexcitation with linear polarized light in dipol approximation

$$\frac{d\sigma_i}{d\Omega} = \frac{\sigma_i}{4\pi}\left[1 + \beta P_2\left(\cos\theta_z\right)\right]. \tag{9}$$

Therein, $P_2(\cos\theta_z)$ is the second Legendre polynomial $P_2(\cos\theta) = \frac{1}{2}\left(3\cos^2\theta - 1\right)$ and θ_z is the angle between the polarization direction (z-axis) of the excitation source and the emission direction of the photoelectron. Tabulated values for β can be found in literature.[55, 56, 57]

For the publications comprising this thesis, linear polarized light was used for spectra recorded at synchrotron facilities, e.g. for the EMIL beamline $\theta_z = 49°$. In contrast to this, laboratory based excitation sources typically provide non-polarized light, it is however possible to transfer Equation 9 to this situation. Just as unpolarized light can be considered to consist of two equal parts of light polarized in orthogonal directions, the photoemission cross section for the photo excitation with unpolarized light propagating in y direction, can be understood as the combination of two photoionization cross sections for light polarized in the z direction and light polarized in the x direction:

$$\begin{aligned}\left.\frac{d\sigma_i}{d\Omega}\right|_{\text{unpol.}} &= \frac{1}{2}\left.\frac{d\sigma_i}{d\Omega}\right|_{\text{pol. along z}} + \frac{1}{2}\left.\frac{d\sigma_i}{d\Omega}\right|_{\text{pol. along x}} \\ &= \frac{\sigma_i}{4\pi}\left[1 - \frac{\beta}{2}P_2(\cos\theta_y)\right].\end{aligned} \tag{10}$$

For the derivation, the relation between the angles, $\cos^2\theta_x + \cos^2\theta_y + \cos^2\theta_z = 1$, was used. In the resulting equation θ_y is the angle between the propagation direction of the unpolarized light and the direction of electron emission.[64]

Figure 7 shows the angle-dependent term of Equation 9 in 7a and the angle-dependent term of Equation 10 in 7b, both for Ga M shell core levels in polar coordinates. At several

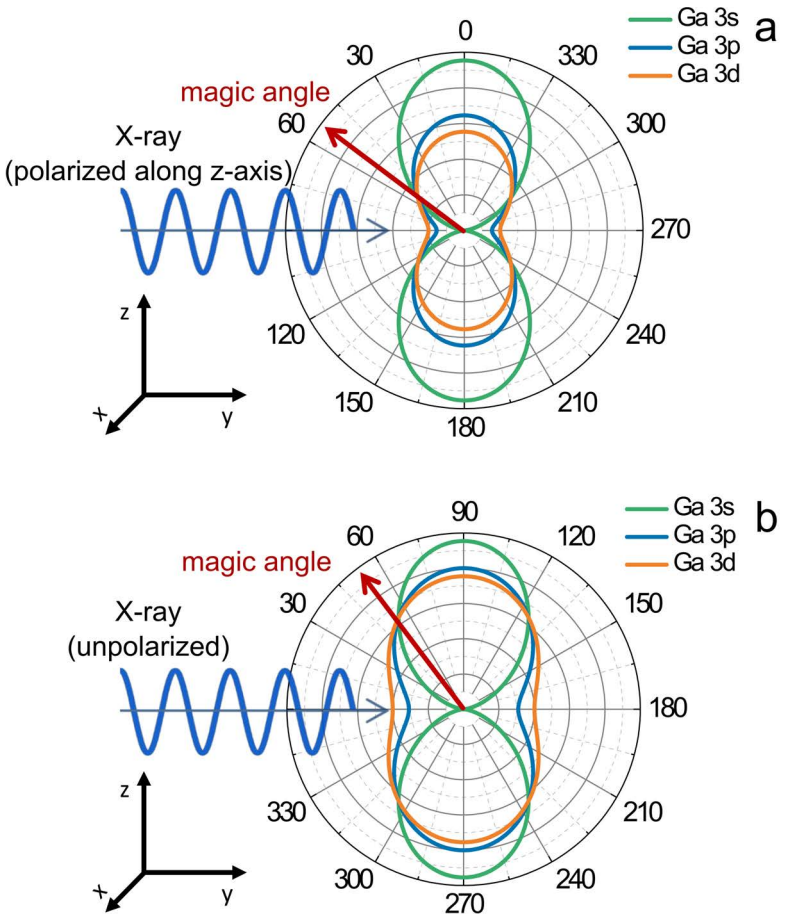

Figure 7 Photoelectron angular distribution for the β-parameters of the Ga M shell core levels (Ga 3s, Ga 3p, Ga 3d). (a) Shows the angular part of Equation 9, more precisely $[1 + \beta P_2 (\cos\theta_z)]$ for excitation with light polarized in z-direction. (b) Shows the angular part of Equation 10, more precisely $\left[1 - \frac{\beta}{2} P_2(\cos\theta_y)\right]$ for excitation with non-polarized light propagating in y-direction.

points, the shown photoelectron angular distributions lines cross each other, this happens at points were, in each case, the angle-dependent terms become zero. These positions are referred to as magic angle and are located e.g. at the $\theta_m \approx 54.74°$, where $\cos^2(54.74°) = \frac{1}{3}$ and therefore $P_2(\cos(54.74°)) = \frac{1}{2}\left(3\cos^2(54.74°) - 1\right) = 0$.

For the results presented in this thesis, such corrections were taken into account for the quantification of high-resolution synchrotron XP spectra measured at EMIL, which are presented in Chapter 4.4.

3 Instrumentation, data processing and materials

3.1 The GAP instrument - laboratory near-ambient pressure XPS

The studies on macroscopic liquid alloy systems [26, 35, 50, 51] were conducted on the GAP instrument, a near-ambient pressure capable XPS setup at the Chair of Physical Chemistry II at the Friedrich-Alexander-Universität Erlangen-Nürnberg. It was constructed between 2000 and 2004 by Jörg Pantförder as part of his PhD thesis.[65] The near-ambient pressure capability of the instrument is employed for the investigation of material relevant for catalysis, in the pressure range from 10^{-10} to 1 mbar. These types of studies contribute to "bridging the pressure and material gap", hence the instruments name. It is well suited for the investigation of liquid samples since the transfer system and measurement geometry allow for keeping the sample horizontal during all transfer, preparation and measurement steps.

The excitation source is a non-monochromatized double anode Al/Mg X-ray tube (Specs XR50-HP) that is kept in UHV by a turbo molecular pump and separated from the analysis chamber by an X-ray window (Specs Si_3N_4 window) sealed by a Viton gasket. Spectra are recorded in normal emission geometry ($\gamma = 0°$ in Equation 5 and following). The angle between the x-ray source and detection-direction is $\theta_y = 65°$. This corresponds roughly to magic angle geometry, which is assumed for quantification. Emitted photoelectrons pass through two differential pumping stages separated from the analysis chamber and each other by apertures before reaching the lens entrance of a modified Omicron EA125 analyzer with increased working distance. The EA125 utilizes electrostatic lenses to focus and decelerate/accelerate photoelectrons and a concentric hemispherical analyzer (CHA) to select specific kinetic energies.[66] For signal detection, a unit of seven channel electron multipliers (Channeltrons) is used. All presented measurements conducted on the GAP setup were performed in constant analyzer energy (CAE) mode. In this mode of operation, only electrons at a specific kinetic energies (pass energy) can pass the CHA to reach the detector, and the spectrum is scanned by using a varying retarding/accelerating voltage before the CHA.

The analysis chamber, both differential pumping stages and the analyzer are all pumped by individual turbo molecular pumps. The analysis chamber is coupled via a transfer system to a load lock and a separated chamber dedicated to sample preparation, the "prep-chamber". In both the analysis and preparation chamber, samples can be heated resistively and cooled by circulating water or liquid nitrogen through the manipulator. Temperature readout by a type K thermocouple is possible and controlled heating/cooling sequences can be programmed and monitored by a Eurotherm 3216. Analysis and prep-chamber are equipped with quadrupol mass spectrometers (Pfeiffer Vacuum, 2x QMA 200 with QME200 and QME220) for gas-phase analysis and reaction gas monitoring. Additionally, the preparation chamber is equipped with a sputter gun for Ar^+ sputtering (Specs IQE-11-A Ion source), a low energy electron diffraction setup (Varian Four Grid LEED Optics) and a quartz crystal microbalance (Syncon 100/MF). A three-pocket evaporator (Omicron EFM 3T) for physical vapor deposition can be mounted to the chamber in a geometry that allows for evaporation of liquids like Ga. For additional details on the setup see [65] and [67].

3.2 Synchrotron XPS at BESSY II - SISSY I, EMIL

The synchrotron-based XPS studies investigating GaRh particles on a flat model support[50], and the surface characterization of GaRh intermetallic phases[68] were conducted at the SISSY I synchrotron end-station for XPS and HAXPES located at the Energy Materials In-Situ Laboratory (EMIL) of the Helmholtz Zentrum Berlin. The measurements were conducted with a CHA (Scienta EW 4000 electron energy analyzer) in CAE mode. Remarkable about this end-station is the dual-color beamline, depending on the experimental needs, soft or hard X-rays can be supplied either by a UE48 undulator with a plane-grating monochromator (PGM) for 80-1800 eV, or by a U17 undulator with a double crystal monochromator (DCM) for 1800 - 10000 eV. Both provide high photon flux and can be focused on the same spot, with a spot size in the micrometer range. The wide energy range and the combination of soft and hard X-rays allows for advanced depth profiling of layered samples or buried interfaces.[69]

The analysis chamber is attached to an automated transfer system with a load lock, sample storage, and a preparation chamber (all Prevac). For sample cleaning and preparation, a sputter gun, sample heating and a three-pocket metal evaporator are available.

The whole system operates in UHV (10^{-9} mbar). Sample transfer between preparation chamber and analysis chamber is possible without breaking vacuum.

3.3 Synchrotron ambient pressure XPS - MAX IV HIPPIE

The studies investigating the adsorption of carbon monoxide on GaPt particles on model supports[29] were performed at HIPPIE, a synchrotron end-station for ambient pressure XPS at MAX IV (Lund, Sweden).[70] Soft X-rays are provided by an Apple 2 type undulator with a PGM that provides high photon flux for photon energies between 250 and 2200 eV. The system utilizes an additional high-pressure cell within the analysis chamber referred to as Catalysis Cell.[71] This way, XPS measurements at pressures up to 10 mbar are possible. An additional important feature of this end-station is the possibility to simultaneously record XP spectra and polarization-modulated infrared reflection absorption spectra (PM-IRAS). For this purpose, infrared translucent windows were build into the Catalysis Cell and the analysis chamber.

The analysis chamber is connected via a transfer system with a load lock, sample storage and a preparation chamber. For sample preparation, multiple metal evaporators can be attached to the preparation chamber, including in geometries that allow for the evaporation of liquid samples like Ga. Apart from ambient pressure measurements in the Catalysis Cell, the system operates in UHV (10^{-9} mbar).

3.4 Software and data processing

The software package Casa XPS 2.3 was used to process all XP spectra presented in this thesis and the herein introduced publications. This includes binding energy correction, fitting baselines and signal deconvolution. Whenever possible, a fit of the Fermi edge, as is described in the Fundamentals section, Figure 4 and Equation 2, was used to calibrate the binding energy scale. When the intensity close to E_F is too low for such a correction, well identifiable XPS signals such as the C 1s signal of highly oriented pyrolytic graphite (HOPG) were used and compared to literature values.[72] From all spectra, linear backgrounds were subtracted. To deconvolute recorded XP spectra, the chosen peak models were fitted using the Levenberg-Marquardt-algorithm implemented in Casa XPS.[73] Symmetric lineshapes were reproduced using Lorentzian/Gaussian product functions[74]; these are implemented as GL in Casa XPS.[75] Asymmetric lineshapes

are especially relevant for metallic samples.[76, 77] For the presented measurements, such signals were approximated using the LF lineshape implemented in Casa XPS.[78, 79, 80] The LF lineshape can reproduce an asymmetry similar to that of the commonly used Doniach-Sunjic (DS) lineshape and is therefore well suited to fit signals of metallic samples. In addition, LF is more versatile compared to DS: e.g. the Ga 3d and Ga $2p_{3/2}$ signals can have peculiar asymmetries, depending on the experimental resolution, which can be hard to reproduce by the DS lineshape, but, in all cases presented in this thesis, good fits were obtained using the LF lineshape.

For graphing, the software package Origin Lab (Origin 9.1, Origin 2019 and following) was used. Due to the large amount of data generated in some experiments, repetitive tasks like the subtraction of baselines were automatized using Python 3 with the packages NUMPY and PANDAS.

For the presented work on the temperature-dependent XPS studies, linear cooling ramps were controlled by a Eurotherm 3216 proportional-integral-derivative controller (PID controller). The necessary parameters of the Eurotherm 3216 were accessed using the software iTools OPC server (V9.68). To read out temperature data and to record the temperature-time curves, iTools OPC scope (V9.68) was used.

3.5 Used materials and sample preparation

Gallium 99.99999% by Sigma-Aldrich/Alfa Aesar, rhodium wire (99.9% Goodfellow), palladium wire, platinum wire (99.95 Alfa Aesar), indium wire (Goodfellow 99.999%) were used for sample preparation. As XPS references, Rh(111), Pt(111) and Pd(111) were used (all MaTecK). For the preparation of macroscopic alloy samples as are shown in Figures 8a and b, the synthesis route outlined by Grabau was used.[25] In short, the components are weighed into a tungsten crucible (12 mm, Kurt Lesker GmbH) mounted to the GAP sample holder. Due to preparation in air, the surface of the alloy is oxidized. To remove the formed Ga_2O_3 and other surface impurities, annealing to 800 K in UHV is often sufficient. At this temperature, in the presence of metallic Ga, the following comproportionation reaction occurs:

$$Ga_2O_3 + 4\,Ga \longrightarrow 3\,Ga_2O$$

Ga_2O_3 reacts with liquid metallic Ga forming the suboxide Ga_2O. Ga_2O is volatile and desorbs to create a metallic Ga surface. For this reaction, significant volatization has

been reported at 930 K in an inert gas stream at 1 bar or in rough vacuum (rotary vane pump).[81, 82] In UHV, we observe fast desorption of the oxide film at approximately 780 K. To keep the formed metallic Ga surface oxide-free UHV is necessary. Already at oxygen partial pressures of 10^{-9} mbar low dimensional Ga_2O_3 structures form on freshly cleaned Ga.[83] To remove further impurities and to improve wetting of the liquid alloy to the tungsten crucible, the sample is sputtered with Ar^+ during annealing. This is especially necessary when working with GaIn alloys, which typically can not be cleaned with just heating alone. This procedure results in clean alloy surfaces as seen by XPS. For oxidation studies, molecular O_2 (Linde 4.7, 99.9997%) was used. After each oxidation experiment, it was possible to fully desorb the formed oxide film by heating the sample to 800 K.

For the preparation of intermetallic Ga_9Rh_2 and Ga_3Rh phases, Figure 8c and d, stoichiometric amounts of Ga and Rh were weighed into Al_2O_3 crucibles (Almath 13 mm x 10.5 mm) in air. To avoid excessive oxidation during preparation, a UHV oven at the chair of Kristallographie und Strukturphysik (Prof. Unruh) at FAU was used that allowed for heating the materials to temperatures of up to 1000°C. After preparation, transport and bulk characterization by X-ray diffraction XRD was performed in air. After introduction to UHV, it was possible to clean the samples by heating, for more details see Chapter 4.4.

GaRh and GaPt particles were prepared by sequential physical vapor deposition of the elements. To simulate the local environment of SiO_2 supported particles and to investigate the particle/oxide interaction, we used the native oxide of a p-doped Si wafer with (100) cut (CrysTek) as flat model support. TEM micrographs of such GaRh nano particles on SiO_2-based grids are shown in Figures 8e and f. As alternative flat model support highly oriented pyrolytic graphite (MikroMasch) was used. Due to its reflectivity properties, this material is better suited for combined XPS and PM-IRAS studies.

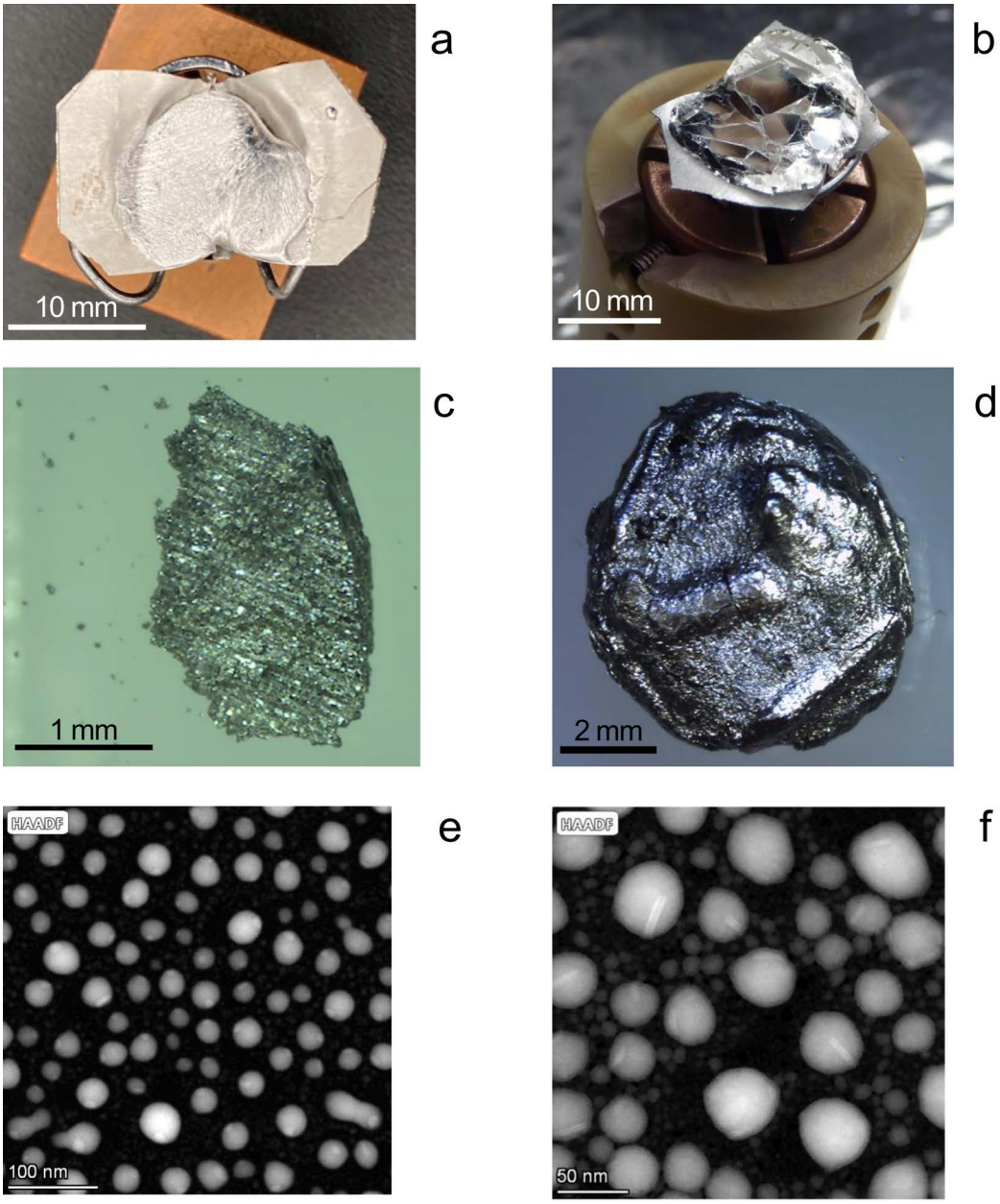

Figure 8 Examples of the samples systems used for the research presented in this thesis: In (a) and (b) macroscopic Ga-alloy samples in tungsten crucibles are shown, in (b) GaPd intermetallics have crystallized on the sample surface. Figures (c) and (d) show GaRh intermetallic phases: (c) Ga_9Rh_2; (d) Ga_3Rh. In (e) and (f) TEM micrographs of physical vapor deposition-prepared GaRh particles supported on TEM grids are shown; intermetallic phases within the particles can be seen as brighter rod-like structures.

4 Introduction to the publications

4.1 Authors contributions to the publications

This Chapter introduces to the authors contributions to the published work on Ga alloys in the context of SCALMS catalysis. It builds on the work of Mathias Grabau and directly continues his studies on the XPS characterization of macroscopic Ga-transition metal model alloys, their phase transition behavior, and their surface oxidation.[24, 25, 32, 84] XPS studies on the oxidation of macroscopic GaRh and GaPd are presented. Beyond this, XPS studies are extended to GaRh and GaPd particles on flat model supports, the phase transition behavior of binary, macroscopic GaIn alloys, and the synthesis and XPS characterization of two GaRh intermetallic phases. This thesis comprises the authors contributions to the following publications:

Publication 1 Haiko Wittkämper, Sven Maisel, Mingjian Wu, Johannes Frisch, Regan G. Wilks, Mathias Grabau, Erdmann Spiecker, Marcus Bär, Andreas Görling, Hans-Peter Steinrück, and Christian Papp, Oxidation induced restructuring of Rh-Ga SCALMS model catalyst systems *The Journal of Chemical Physics* 153, 104702-12 (2020).
(`https://aip.scitation.org/doi/10.1063/5.0021647`)

Publication 2 Haiko Wittkämper, Sven Maisel, Michael Moritz, Mathias Grabau, Andreas Görling, Hans-Peter Steinrück, and Christian Papp, Surface oxidation-induced restructuring of liquid Pd-Ga SCALMS model catalysts *Physical Chemistry Chemical Physics* 23, 16324-16333 (2021).
(`https://pubs.rsc.org/en/content/articlelanding/2021/cp/d1cp02458b`)

Publication 3 Haiko Wittkämper, Sven Maisel, Michael Moritz, Mathias Grabau, Andreas Görling, Hans-Peter Steinrück, Christian Papp, Temperature-dependent XPS studies on Ga-In alloys through the melting-point *Surface Science* 717, 122008 (2022).
(`https://www.sciencedirect.com/science/article/abs/pii/S0039602821002119`)

Publication 4 Haiko Wittkämper, Rainer Hock, Matthias Weißer, Johannes Dallmann, Carola S. Vogel, Narayanan Raman, Nicola Taccardi, Marco Haumann, Peter Wasserscheid, Tzung-En Hsieh, Sven Maisel, Michael Moritz, Christoph Wichmann, Johannes Frisch, Mihaela Gorgoi, Regan G. Wilks, Marcus Bär, Mingjian Wu, Erdmann Spiecker, Andreas Görling, Tobias Unruh, Hans-Peter Steinrück and Christian Papp, Isolated Rh atoms in dehydrogenation catalysis *submitted*, (2022).

Publication 5 Narayanan Raman, Sven Maisel, Mathias Grabau, Nicola Taccardi, Jonas Debuschewitz, Moritz Wolf, Haiko Wittkämper, Tanja Bauer, Mingjian Wu, Marco Haumann, Christian Papp, Andreas Görling, Erdmann Spiecker, Jörg Libuda, Hans-Peter Steinrück, and Peter Wasserscheid, Highly Effective Propane Dehydrogenation Using Ga-Rh Supported Catalytically Active Liquid Metal Solutions *ACS Catalysis* 9, 9499-9507 (2019).
(`https://pubs.acs.org/doi/10.1021/acscatal.9b02459`)

Publication 6 Chantal Hohner, Miroslav Kettner, Corinna Stumm, Dominik Blaumeiser, Haiko Wittkämper, Mathias Grabau, Matthias Schwarz, Christian Schuschke, Yaroslava Lykhach, Christian Papp, Hans-Peter Steinrück, and Jörg Libuda, Pt-Ga Model SCALMS on Modified HOPG: Thermal Behavior and Stability in UHV and under Near-Ambient Conditions *The Journal of Physical Chemistry C* 124, 2562-2573 (2020).
(`https://pubs.acs.org/doi/10.1021/acs.jpcc.9b10944`)

In the following, these publications are abbreviated as P1,..., P6. In more detail, the authors contributions to these papers are:

P1 XPS measurements with Grabau, XPS data evaluation, authorship

P2 XPS measurements with Grabau, XPS data evaluation, authorship

P3 XPS measurements with Grabau, XPS data evaluation, authorship

P4 preparation of GaRh intermetallics with Weißer and Moritz, XPS measurements with Moritz, Hsieh, Wichmann, XPS data evaluation, authorship

P5 XPS measurements with Grabau, coauthorship

P6 XPS measurements with Grabau, XPS data evaluation, coauthorship

4.2 XPS studies on macroscopic transition metal-Ga alloy samples (P1, P2, P5)

This Chapter provides an introduction to results obtained form the photoemission studies on macroscopic GaRh and GaPd alloys with low transition metal content. Starting out with the phase transition behavior of metallic GaRh (P5) and then moving to the oxidation behavior of GaRh (P1) and GaPd (P2).

In situ oxidation of macroscopic GaRh alloy samples (P1)

XPS studies on GaRh based SCALMS catalyst samples clearly show that a reduced GaRh phase forms during catalytic testing. Macroscopic liquid GaRh droplets with concentrations similar to those of the GaRh SCALMS catalysts were chosen as a model system for the observed reduced alloy phase. For all SCALMS catalysts investigated, scanning electron microscopy suggests a wide particle size distribution with particles sizes ranging from a few hundred nanometers up to the micrometer scale.[26, 36] This justifies the use of macroscopic alloy samples since typical nano-scale effects on the XPS binding energies become relevant only for very small particles, e.g. for Rh 2.5 nm and below.[85]

Three macroscopic GaRh alloys with compositions comparable to those of the GaRh based SCALMS catalysts, $Ga_{166}Rh$ (0.6 at.% Rh), $Ga_{82}Rh$ (1.2 at.% Rh) and $Ga_{49}Rh$ (2.0 at.% Rh) were investigated. Temperature-dependent XPS studies starting from room temperature, show that the Rh concentration in the probe volume of XPS increases with temperature. This is attested to a transition from a biphasic state to a fully liquid state. For all three concentrations, the known part of the GaRh phase diagram suggests the precipitation of Ga_9Rh_2 at room temperature. The temperature-dependent surface concentration observed in XPS agrees well with the expected phase transition temperature according to the phase diagram. Notable is a difference between the phase transition temperatures observed in XPS for macroscopic GaRh alloys and microscopic GaRh particles in *in situ* heating TEM experiments, where significantly higher melting temperatures (ΔT up to 50°C) are observed for the nano particles. The characterization of the phase transition behavior of such particle systems is part of ongoing research. For additional details on the XPS characterization of macroscopic GaRh systems see [26, 36] and [25].

The so far introduced *in situ* heating studies have been performed in UHV with an atomically clean metal surface. In the application, a catalyst will be handled in

air and be exposed to traces of oxygen or water from the reactor feed. Ga is highly oxophilic, and will, in presence of water or molecular oxygen readily form Ga oxides with the stoichiometry Ga_2O_3 or the suboxide Ga_2O. Studying the reactivity of the Ga-transition metal alloys towards molecular oxygen, is therefore of high relevance for catalytic application. With this intention, near-ambient pressure XPS measurements were performed using the GAP setup. In a total of ten experiments, a macroscopic $Ga_{125}Rh$ (0.7 at.% Rh in Ga) alloy was measured during exposure to 1 mbar (up to a dose of $4.9{\cdot}10^9$ Langmuir (L) O_2), 10^2 mbar ($1.7{\cdot}10^8$ L O_2), 10^3 mbar ($1.4{\cdot}10^7$ L O_2), 10^5 mbar ($1.1{\cdot}10^5$ L O_2), and 10^7 mbar (700 L O_2) at 550 K and $3{\cdot}10^7$ mbar ($4.4{\cdot}10^3$ L O_2), $3{\cdot}10^5$ mbar ($4.4{\cdot}10^5$ L O_2), and 1 mbar ($8.9{\cdot}10^9$ L O_2) at 300 K.

Figure 9 shows the (a) Ga 3d, (b) Ga $2p_{3/2}$, (c) Rh 3d and (d) O 1s core level regions recorded before (blue line), after (red line) and, *in situ*, during the oxidation (gray lines) of the $Ga_{125}Rh$ alloy. The shown data was collected from the oxidation experiment conducted at 10^2 mbar where the alloy was exposed to a total of $1.7{\cdot}10^8$ L of molecular oxygen at a temperature of 550 K. For the purely metallic surface measured before exposure (blue lines), we see Ga 3d and Ga $2p_{3/2}$ at 18.6 and 1116.7 eV, values that agree well with metallic Ga. In the metallic state, no significant Rh signal is seen, this is because at 300 and 550 K $Ga_{125}Rh$ is expected to be biphasic. According to what is known about the RhGa phase diagram, Rh is expected to be bound in a Ga_9Rh_2 intermetallic phase in the bulk of the droplet, with an expected liquidus temperature between 600 and 800 K. The observed changes in the Ga 3d, Ga $2p_{3/2}$ and O 1s spectra, during and after O_2 exposure, are characteristic for the formation of a Ga oxide overlayer. The intensity of the metallic Ga core levels decreases and additional signals, assigned to Ga oxide, appear and grow at 20.6 eV for Ga 3d (Ga^0 3d + 2.0 eV) and at 1118.7 eV for Ga $2p_{3/2}$ (Ga^0 $2p_{3/2}$ + 2.0 eV). In addition, an O 1s signals grows at 531.5 eV. The shifts of the Ga core levels and the O 1s binding energy are characteristic for Ga_2O_3. Furthermore, a quantification based on the fitted Ga oxide and O 1s components yields a Ga/O ratio of 0.69 for Ga 3d and 0.79 for Ga $2p_{3/2}$, both values are close to the expected ratio of 0.67 for Ga_2O_3. Interesting changes occur in the Rh 3d region. Here, starting out form no significant Rh 3d signal intensity, a well visible Rh 3d signal is detected upon O_2 exposure. The observed binding energy between 307.6 and 308.0 eV is unique and neither fits metallic Rh (307.4 eV) or Rh oxide (308.3 eV and higher).[86, 87]

Figures 9e and 9f show the development of the signals assigned to metallic Ga, Ga in Ga_2O_3, O in Ga_2O_3 and the new Rh species. Examples of the fits are found in the support-

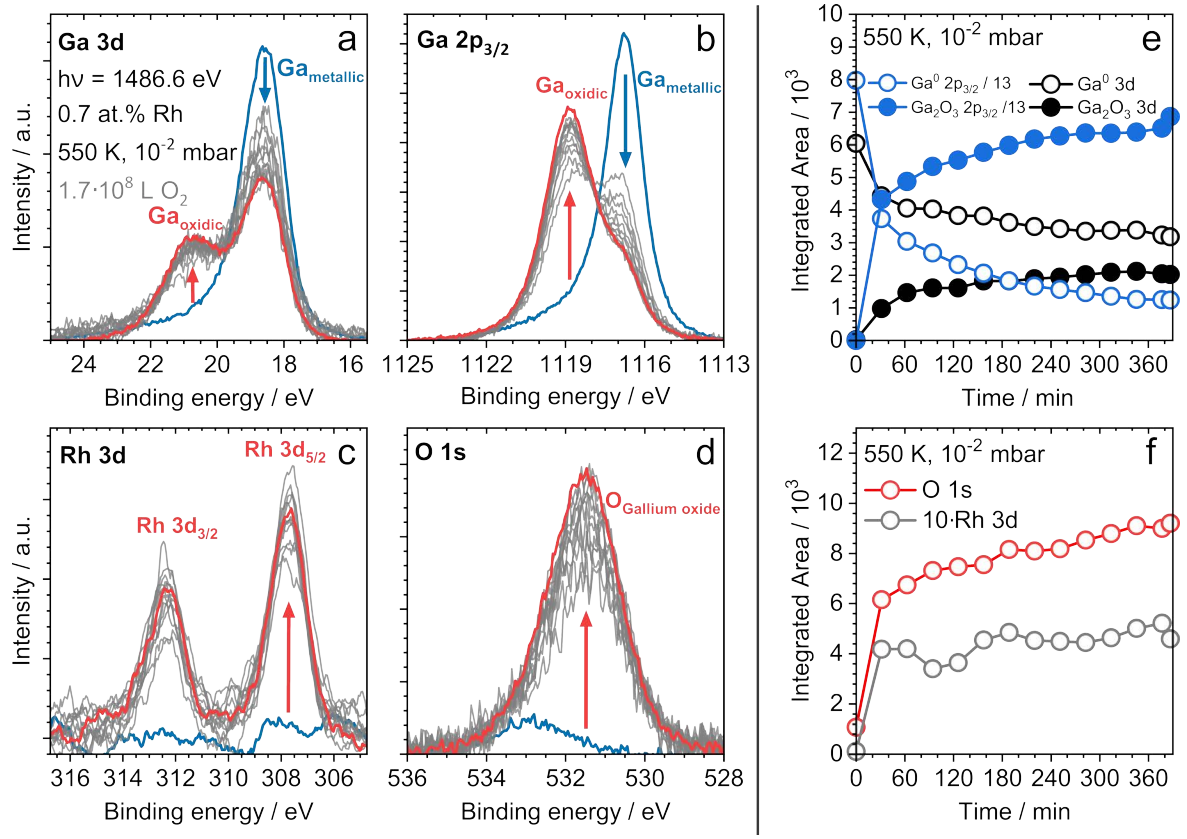

Figure 9 XP spectra recorded before (blue lines), during (gray lines) and after (red lines) the *in situ* exposure of a macroscopic $Ga_{125}Rh$ liquid metal alloy to 10^{-2} mbar O_2 in (a), (b), (c) and (d). In (e) and (f) the quantitative developments of the signal areas assigned to metallic Ga, Ga_2O_3, Rh and O are shown in a times-resolved fashion for better comparison. (Adapted and modified from [50] with permission by AIP Publishing.)

ing information of P1.[88] Noteworthy in Figure 9e is the difference in the Ga_2O_3/Ga^0 ratio between Ga 3d and Ga $2p_{3/2}$. This is due to the difference in surface sensitivity: the Ga 3d signal is more bulk-sensitive (kinetic energy of 1466 eV) and therefore shows a larger metallic Ga component, while the more surface-sensitive Ga $2p_{3/2}$ signal shows a larger oxidic component. The different ratios combined with the difference in surface sensitivity leads to the conclusion that the Ga_2O_3 indeed forms an overlayer on top of the alloy.

Figure 9f shows the development of the O 1s signal assigned to Ga_2O_3 and the newly emerging Rh 3d signals (scaled tenfold for better comparison). Notable is the very similar development during oxidation. Both signals rapidly appear at the start of O_2 exposure and continuously increase with a similar slope during the experiment. To

further investigate the correlation between the forming Ga_2O_3 layer and the emerging Rh 3d signal, the detected Rh content and Ga_2O_3 film thicknesses are compared for all oxidation experiments. The Ga_2O_3 film thickness is calculated based on the Ga_2O_3 to Ga^0 signal area ratios shown in Figure 9e.[89] Starting from Equations 7 and 8, the signal intensity ratio can be expressed as

$$\frac{I^{\mathrm{ol}}_{\mathrm{Ga_2O_3\ Ga\ 3d}}}{I^{\mathrm{bulk}}_{\mathrm{Ga^0\ Ga\ 3d}}} = \frac{\sigma_{\mathrm{Ga\ 3d}} T^{\mathrm{inst.}}_{\mathrm{Ga\ 3d}} J_{\mathrm{h}\nu} n^{\mathrm{ol}}_{\mathrm{Ga}} \left(\lambda^{\mathrm{ol}}_{\mathrm{Ga\ 3d}} - \lambda^{\mathrm{ol}}_{\mathrm{Ga\ 3d}} \exp\left(-\frac{d_{ol}}{\lambda^{\mathrm{ol}}_{\mathrm{Ga\ 3d}}} \right) \right)}{\sigma_{\mathrm{Ga\ 3d}} T^{\mathrm{inst.}}_{\mathrm{Ga\ 3d}} J_{\mathrm{h}\nu} n^{\mathrm{bulk}}_{\mathrm{Ga}} \lambda^{\mathrm{bulk}}_{\mathrm{Ga\ 3d}} \exp\left(-\frac{d_{ol}}{\lambda^{\mathrm{ol}}_{\mathrm{Ga\ 3d}}} \right)},$$

or the corresponding expression for Ga $2p_{3/2}$. Eliminating the common values from the fraction and then solving for the overlayer film thickness d_{ol} yields

$$d_{ol} = \lambda^{\mathrm{ol}}_{\mathrm{Ga\ 3d}} \ln\left(\frac{I^{\mathrm{ol}}_{\mathrm{Ga_2O_3\ Ga\ 3d}} \lambda^{\mathrm{bulk}}_{\mathrm{Ga\ 3d}} n^{\mathrm{bulk}}_{\mathrm{Ga}}}{I^{\mathrm{bulk}}_{\mathrm{Ga^0\ Ga\ 3d}} \lambda^{\mathrm{ol}}_{\mathrm{Ga\ 3d}} n^{\mathrm{ol}}_{\mathrm{Ga}}} + 1 \right), \tag{11}$$

the necessary values for the atom densities n_{Ga} and IMFPs $\lambda_{\mathrm{Ga\ 3d}}$ are listed in the SI of P1.[88]

Figure 10a shows the time development of the Ga_2O_3 film thickness for the oxidation experiments conducted at 550 K; the so far discussed dataset is shown in black. The overall trend of the film development is a very rapid initial film growth followed by a slower almost linear increase of film thickness. Notable is the oxidation at 10^{-7} mbar were no rapid initial film growth is observed; this may point to a different oxide formation mechanism at low pressures. Figures 10b and 10c show the Rh concentration x_{Rh} calculated from the emerging Rh 3d signal and total Ga 3d signal with the increasing film thickness determined from Equation 11. In Figure 10b, both *in situ* (transparent symbols) and UHV (opaque symbols) measurements are shown. Figure 10c only shows measurements recorded after pumping back to UHV for clarity. Overall, an increase of the detected Rh content with increasing film thickness is visible. For Rh, which is located below the forming Ga_2O_3 layer, one would expect an attenuation of the Rh intensity similar to that of metallic Ga. Therefore, the conclusion is that the intensity results from Rh that is incorporated into the forming Ga_2O_3, very similar to what was reported for the oxidation of macroscopic GaPt liquid metal alloys.

For the GaPt system, the incorporation of Pt into Ga_2O_3 was associated with significant binding energy shifts, which is expected due to the significant change in the chemical

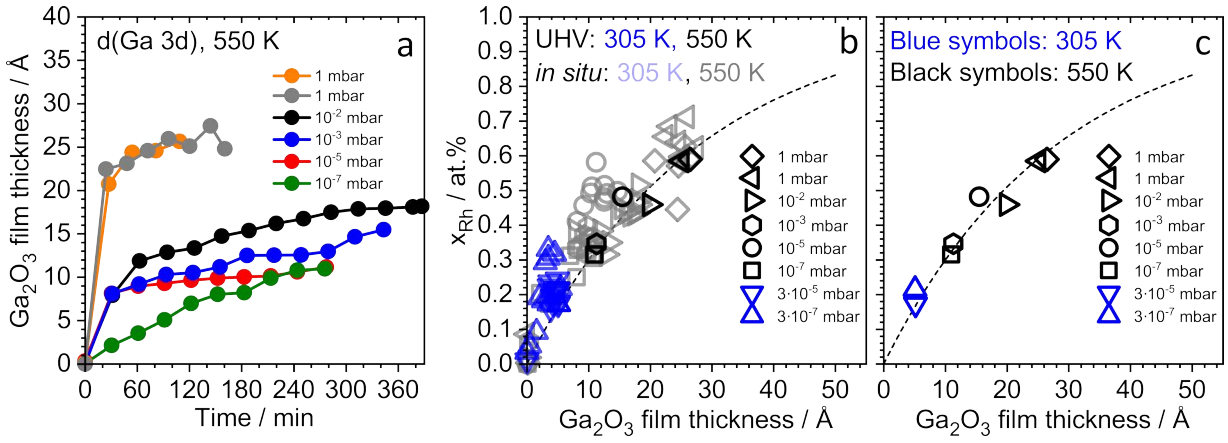

Figure 10 Time development of the oxide film thickness calculated according to Equation 11 in Figure (a). Figures (b) and (c) show the calculated Rh concentration with increasing film thickness, a clear trend is seen that higher Ga_2O_3 film thicknesses correspond to higher Rh concentrations. The dashed line is a guide to the eye. (Adapted and modified from [50] with permission from AIP Publishing.)

environment of the Pt atoms.[32] Therefore, close attention was paid to changes in the binding energies of the Rh and Ga signals during the oxidation. Figure 11 shows a comparison of Rh 3d and Ga 3d XP spectra of pure metal samples in form of a Rh(111) single crystal and pure, liquid Ga (black spectra) to: a fully metallic and liquid $Ga_{125}Rh$ sample at 850 K (orange spectra), a GaRh intermetallic phase (blue spectra), and two oxidized GaRh samples with Ga_2O_3 film thicknesses of 16 Å (green spectra) and 32 Å (red spectra). The GaRh intermetallic phase discussed here was found to occasionally crystallize on top of the biphasic the $Ga_{125}Rh$ alloy, based on the binding energy and XPS quantification it is likely Ga_9Rh_2, $Ga_{16}Rh_3$, or $Ga_{21}Rh_4$. A clear differentiation of these phases is not possible purely based on XPS due their similar composition and small relative binding energy shifts as predicted by DFT. The measured Rh 3d spectra show spin-orbit-split doublets, in all cases, the intensity ratio matches the expectation for a 3d signal and the spin-orbit splitting corresponds to the literature value of 4.74 eV.[87] For all following spectra, Rh 3d shifts are given relative to the Rh(111) measurement, for which a binding energy of 307.4 eV is observed. The asymmetry of the Rh signals is slightly reduced upon alloying. A similar reduction in asymmetry is also seen for GaRh particles and GaRh intermetallic phases discussed in the following Chapters. A general peculiarity of the Rh(111) XP spectrum is that the Rh $3d_{3/2}$ component shows a higher FWHM compared to the Rh $3d_{5/2}$ component. This is ascribed to a Coster-Kronig M_4M_5V decay of the M_4 ($3d_{3/2}$) core hole.[90] Noteworthy is that this transition seems

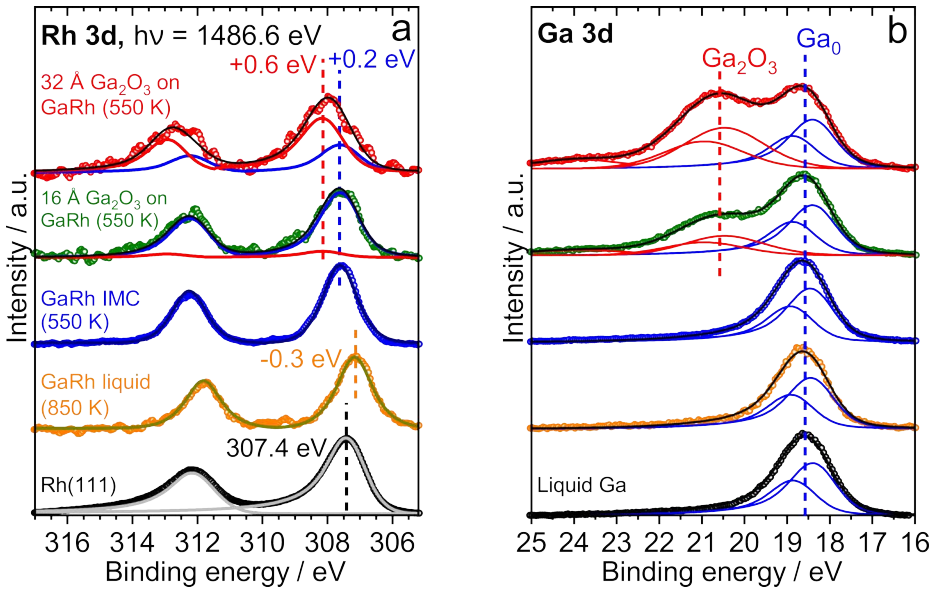

Figure 11 Comparison of the observed (a) Rh 3d and (b) Ga 3d spectra for five GaRh-SCALMS relevant systems: Starting from the bottom with pure metal references, a fully liquid $Ga_{125}Rh$ alloy at 850 K, a intermetallic phase and two oxidized GaRh alloy systems. For better comparison, the spectra are height normalized. (Adapted and modified from [50] with permission from AIP Publishing.)

chemistry sensitive. In all following cases, where Rh is alloyed with Ga, the Rh $3d_{3/2}$ and Rh $3d_{5/2}$ FWHM are exactly equal. The Rh 3d FWHM therefore, besides the binding energy, presents additional indication whether Rh is alloyed or not.

The Ga 3d spectrum of elemental Ga shows a signal peak at 18.6 eV. Generally for the shown Ga spectra, the spin-orbit splitting is not resolved. Nevertheless, a fit model with two components was used to reproduce the signal envelope. The Ga $3d_{5/2}$ component of metallic Ga is found at 18.4 eV for all Ga 3d spectra in Figure 11b. For the fully liquid $Ga_{125}Rh$ at 850 K (orange spectrum), a shift to negative binding energies by -0.3 eV is found. This hints at a charge transfer from Ga to Rh. Such a charge transfer is expected according to the electronegativites of the elements (Pauling Scale: Ga 1.6, Rh 2.2)[49] and also predicted by *ab initio* MD (P1). It was, however, not possible to reproduce the measured binding energy for the fully liquid alloy by the *ab initio* MD presented in P1. The GaRh intermetallic phase shows a small shift to higher binding energies by +0.2 eV that agrees with DFT-calculated binding energies for $Ga_{16}Rh_3$ and $Ga_{21}Rh_4$ (P1), but also Ga_9Rh_2 (P4). A more detailed discussion follows in the next two Chapters.

The shown oxidized spectra were measured on an alloy with a 16 Å Ga_2O_3 overlayer (green spectra) obtained by oxidizing the $Ga_{125}Rh$ alloy at 10^{-2} mbar O_2. Similarly, a

system with a 32 Å Ga_2O_3 overlayer (red spectra) was obtained by oxidizing the $Ga_{125}Rh$ alloy more rapidly at 1 mbar. The Ga 3d spectra of both systems with oxide overlayers show the typical components characteristic for Ga_2O_3, shifted by +2 eV to higher binding energy compared to the metallic Ga signals. Over the whole oxidation experiment, Rh 3d signals for the oxidized GaRh systems generally shift between +0.6 and +0.2 eV to higher binding energies. Shown in Figure 11a, the green and red spectra, are two extreme cases where Rh $3d_{5/2}$ is mostly at 307.6 eV (16 Å Ga_2O_3) and mostly at 308.0 eV (32 Å Ga_2O_3). The signal envelopes of all recorded Rh 3d spectra can be reproduced with high accuracy when using two components at 307.6 and 308.0 eV. Comparison with the shown GaRh intermetallic phase spectrum leads to the conclusion that the 307.6 eV component in the oxidized systems likely originates from GaRh intermetallic phases Ga_9Rh_2, $Ga_{16}Rh_3$, or $Ga_{21}Rh_4$. It is possible that the forming Ga/Ga_2O_3 interface provides a advantageous nucleation site to form intermetallic crystallites. Possibly, these crystallites are even incorporated into the forming Ga_2O_3. High-resolution synchrotron XPS measurements on supported GaRh particles combined with density functional theory calculations suggest that the 308.0 eV component originates from Rh atoms incorporated into octahedral sites of the Ga_2O_3 lattice. Further results on the incorporation of Rh in Ga_2O_3 are presented in the discussion of supported GaRh particles.

In situ oxidation of macroscopic GaPd alloy samples (P2)

Besides the *in situ* oxidation studies on pure Ga and GaPt published by Grabau et al.[32], and the GaRh oxidation studies presented so far, near-ambient pressure oxidation studies for the GaPd system were conducted. The experimental settings were similar to those presented before: The experiments were performed using the GAP setup. Two macroscopic GaPd alloys with 1.3 and 1.8 at% Pd content were oxidized by exposure to molecular O_2 at 550 K and simultaneously measured by XPS.

Similar to the GaPt and the GaRh systems, the formation of a Ga/Ga_2O_3 interface results in a restructuring of the Pd distribution in the alloy. As an initial reaction to the oxidation, the detected Pd signals increase, suggesting that Pd is pulled to the surface. However, with ongoing oxidation the detected Pd signal decreases, in the same fashion as the metallic Ga 3d signal. This suggests that the growing oxide film attenuates the photoemission signals of Pd. Hence, in contrast to the GaPt and the GaRh systems, Pd seems not to be incorporated into the forming oxide film but enriches below the oxide. For more details on the development of the Ga 3d, Ga $2p_{3/2}$, O 1s and Pd 3d spectroscopic

regions and the quantitative component development during the *in situ* oxidation of liquid GaPd, the reader is referred to the dissertation of Mathias Grabau [25] and P2.

Here, the discussion is focused on the binding energies observed for the GaPd system. Figure 12 shows a direct comparison of the Pd 3d and Ga 3d binding energies recorded from pure element references (black), the Ga_5Pd intermetallic phase (red), a fully liquid GaPd sample (blue) and an oxidized Pd Ga sample (orange). For the metallic (111) facet

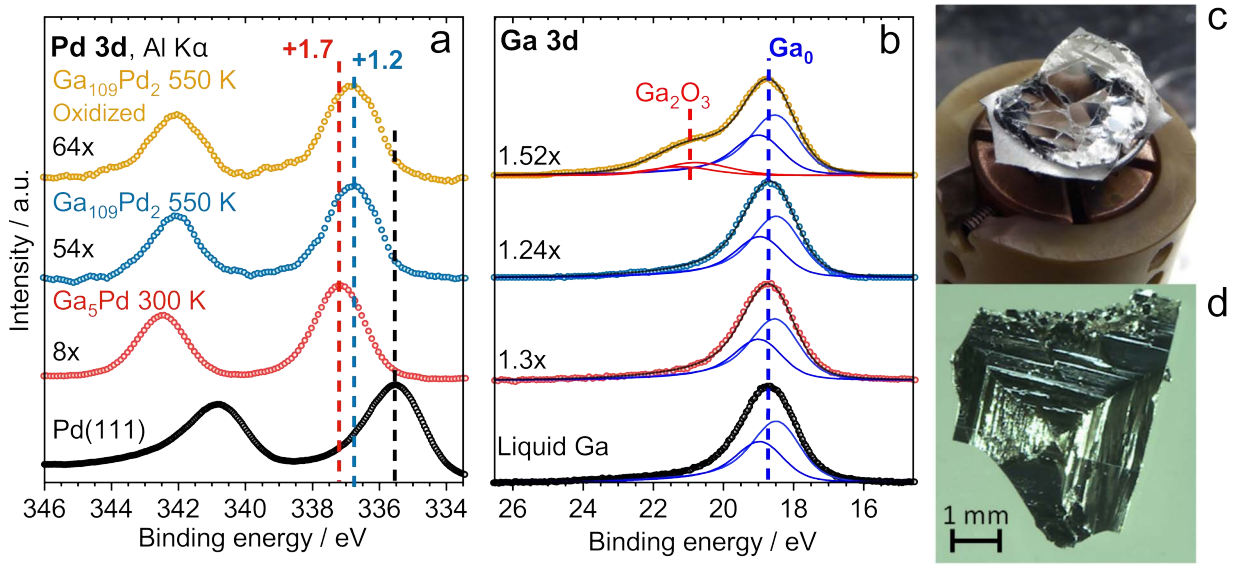

Figure 12 Comparison of the observed (a) Pd 3d and (b) Ga 3d binding energies for pure metal references (Liquid Ga and Pd(111)) and three GaPd systems: A Ga_5Pd intermetallic phase that crystallized on top of the liquid alloy; the fully liquid $Ga_{109}Pd_2$ alloy at 550 K; and a oxidized $Ga_{109}Pd_2$ alloy at 550 K. Additionally, two pictures of the solid Ga_5Pd are shown. For better comparison, the spectra are height normalized. (c) Shows the Ga_5Pd intermetallic phase crystallized on the liquid $Ga_{109}Pd_2$ sample, under the light microscope (d) crystal facets are well visible. ((a) and (b) adapted and modified from [51] with permission from PCCP Owner Societies.)

of Pd, the observed Pd 3d signal shows a spin-orbit-split doublet with an asymmetric line shape and the Pd $3d_{5/2}$ component at 335.6 eV. For all samples the binding energy of the Ga 3d core levels was 18.4 eV, as is also found for metallic Ga. In all shown spectra of GaPd systems, the Pd 3d line shape becomes less asymmetric and shifts to higher binding energies compared to the Pd(111) reference. The highest shift of +1.7 eV is observed for the Ga_5Pd phase. During the work with the liquid GaPd alloy the precipitation of this solid phase on top of the melt (Figure 12c, d) was regularly observed. XPS quantification of such crystals result repeatedly and with good accuracy at a Ga_5Pd stoichiometry, which matches the thermodynamically expected intermetallic phase according to the GaPd

phase diagram.[91, 92] Regarding the binding energy, this phase can be differentiated from the fully liquid $Ga_{109}Pd_2$ alloy and the oxidized $Ga_{109}Pd_2$ alloy, where smaller shifts of +1.2 eV are observed. Compared to the $Ga_{125}Rh$ system, the $Ga_{109}Pd_2$ is expected to be fully liquid at 550 K. Therefore, a significant Pd 3d signal is visible even before oxidation. Furthermore, in contrast to GaRh system, it is not possible to identify contributions of intermetallic phases or unique binding energies for the oxidized GaPd system. Regarding the binding energy, the observed enrichment of Pd below the Ga_2O_3/Ga interface most likely results in an increased Pd concentration in the liquid GaPd layer below the interface.

This is supported by *ab initio* MD simulations, which suggest that Pd atoms in a liquid GaPd phase below a solid Ga_2O_3 layer tend to move to the Ga_2O_3/Ga interface and enrich in the first liquid Ga layer below the interface. In addition, the calculations reproduce the observed XPS binding energy shifts with good accuracy. Despite that, they show a charge transfer form Ga to Pd, the calculated XPS shifts match the measured shifts to higher binding energy well. The reason is a final-state effect as described in Chapter 2.2: The alloying of Pd and Ga results in significant changes in the valence electronic structure compared to the pure metals, which largely improves the screening of the generated core hole, resulting in a large positive $\delta_{\text{relaxation}}$ (compare Equation 4) that, in turn, results in a positive binding energy shift. For more details on these calculations see P2, the supporting information of P2 and the dissertation of Sven Maisel[93].

The working hypothesis is that the differences in the oxidation behavior of the GaRh and the GaPd systems results from the different phase states the systems are in. At 550 K the investigated GaPd systems are fully liquid, while the investigated GaRh systems are biphasic. If the incorporation of Rh in to Ga_2O_3 is a result of the decomposition of GaRh intermetallic phases, the absence of similar phases in the fully liquid GaPd system may well explain why an incorporation of Pd into the forming Ga_2O_3 is not found. Further research investigating such oxidation experiments in connection with the phase-state of the Ga-transition metal alloy is currently in progress.

4.3 GaRh and GaPt particles on flat model supports (P1, P5, P6)

Until now (Mar. 2022), understanding the particle size distribution of the Ga-transition metal alloys of real SCALMS catalysts is a matter of ongoing research. Though it is still an open question, which type of model system would describe the real catalyst best, binary GaRh and GaPt nano-alloy particles on flat model supports were chosen as a starting point for the investigations. Besides studying the particle to support interaction, it is necessary to check for possible size effects that can significantly influence the properties of binary nano-alloys.[94] In contrast to the macroscopic liquid alloys, these types of model systems are accessible to TEM and to measurements at synchrotron endstations, which require non-horizontal sample mounting during transfer or measurement.

The first supported model particle studies on the SCALMS systems were TEM measurements with GaRh particles on SiO_2- and SiN-based TEM grids. In addition to TEM imaging, *in situ* heating studies, small angle electron diffraction (SAED) and high resolution energy dispersive x-ray (EDX) studies were conducted on the GaRh particles. Similar to what was observed for the macroscopic alloy system in XPS, the particles are biphasic, consisting of a mostly Rh-depleted liquid and Rh-rich intermetallic crystallites. In contrast to what is expected according to the known part of the GaRh phase diagram, SAED suggests $Ga_{16}Rh_3$ or $Ga_{21}Rh_4$ for the crystalline phases. For additional details, the reader is referred to P5 and the supporting information of P5.

As a next step, the oxidation of the supported nano GaRh alloy was investigated. GaRh particles with low Rh content (<2.5 at.%) were deposited by physical vapor deposition onto the native oxide of a SiO_2/Si(100) wafer and investigated by synchrotron XPS at the SISSY 1 endstation. The SiO_2/Si(100) oxide presents a well defined model support for which good comparability to TEM results obtained on SiO_2 TEM grids is expected. The particles were prepared by the subsequent deposition of 2.2 Å Rh, followed by 123 Å Ga. Finally, the particles were oxidized by exposure to air. High resolution XP spectra at 449, 1045 and 1500 eV photon energy were recorded after each deposition step and after oxidation. All measurements were conducted at room temperature.

Figure 13 shows the spectra recorded at 449 eV photon energy. In 13a the spectra of the Rh 3d region and in 13b the spectra of the Ga 3d region are shown. The experimental steps are listed from top to bottom: Starting from pure Rh particles deposited on the model support (top), moving to GaRh particles (mid) and finally the oxidized particle system (bottom). Figure 13c shows a TEM micrograph of a oxidized GaRh particle obtained by the same preparation route on a SiO_2 based TEM grid.

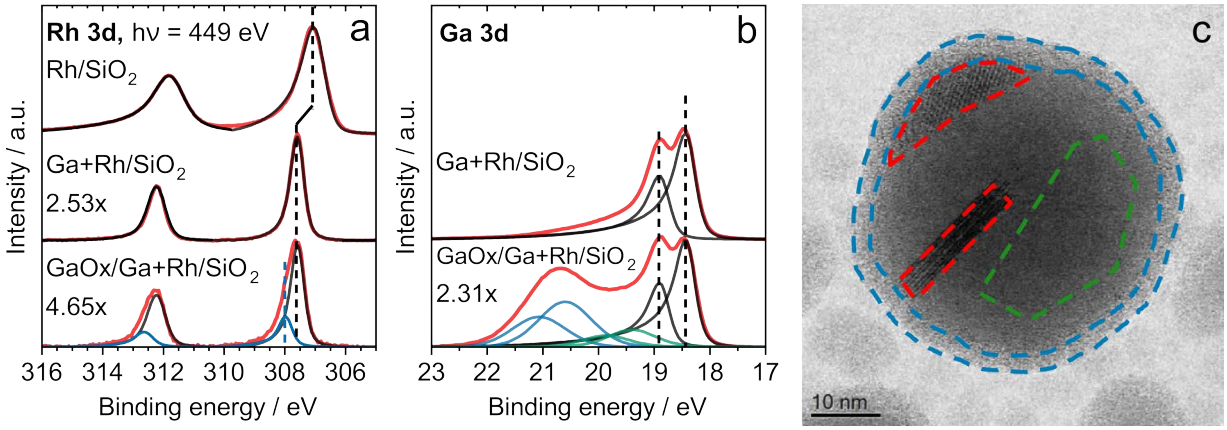

Figure 13 High-resolution synchrotron XP spectra of (a) the Rh 3d and (b) the Ga 3d region recorded during the preparation and subsequent oxidation of GaRh nano-particles on a flat SiO_2/Si(100) model support. Starting from the top in (a), a spectrum of pure Rh particles is shown, followed by spectra of the metallic GaRh particle system (mid) and the particle system after exposure to air (bottom). (c) Shows a high-magnification TEM image of a similar GaRh particle deposited by physical vapor deposition on a SiO_2 TEM grid and oxidized in air. The dashed lines indicate Rh-depleted Ga (green), GaRh intermetallic phases (red) and a Ga_2O_3 layer around the particle (blue). (Adapted and modified from [50] with permission from AIP Publishing.)

For pure Rh particles on SiO_2 (Figure 13a, top), the spin-orbit-split Rh 3d doublet with Rh $3d_{5/2}$ at a binding energy of 307.0 eV is observed. In comparison, a Rh(111) single crystal shows a Rh $3d_{5/2}$ binding energy of 307.4 eV. A likely explanation are under-coordinated Rh atoms[95, 96, 97] or the interactions between the Rh particles and the SiO_2 substrate[98]. The line shape is distinctly asymmetric and the signals show a high FWHM, while the Rh $3d_{3/2}$ component show a larger FWHM (1.24 eV) than the $Rh_{5/2}$ component (0.84 eV), as is typical for non-alloyed Rh.

After Ga deposition (Figure 13a and b, mid), the Rh $3d_{5/2}$ signal shifts by +0.6 eV to higher binding energy, to 307.6 eV. The lineshape becomes less asymmetric and the peaks narrow (FWHM 0.52 eV); now both $Rh_{5/2}$ and Rh $3d_{3/2}$ show the same FWHM. Both the loss in asymmetry and the equivalent peak width indicate alloying. The loss in asymmetry is attested to changes in the valence band of the GaRh alloy, more precisely, a reduced density of states at the valence band edge compared to the pure metal systems. This is described for the GaPd system in literature.[99, 100, 101] Additional details, including valence band calculations for $Ga_{16}Rh_3$ and $Ga_{21}Rh_4$, are given in P1. Based on the microscopic picture of such GaRh particles, which was provided by the TEM studies, and based on the temperature-dependent XPS studies on the macroscopic GaRh systems,

the precipitation of intermetallic phases is expected at room temperature. In contrast to the macroscopic GaRh alloy discussed in the previous Chapter, here a significant amount of Rh is visible even at room temperature. This is explained by the particle size. While in the macroscopic system, Rh-rich phases tend to crystallize in the bulk or at the bottom of the droplet and are thereby removed from the probe volume of XPS, the small particle size of the supported particles results in an increased amount of Rh-rich phases in the XPS interaction volume. The measured binding energy of 307.6 eV perfectly matches the previously observed binding energy for the GaRh intermetallic phase in the macroscopic alloy system. The assignment to a defined intermetallic phase by XPS alone is, however, not possible, as stated in the beginning of this Chapter. SAED from the TEM studies suggests $Ga_{16}Rh_3$ or $Ga_{21}Rh_4$. DFT calculations show that $Ga_{16}Rh_3$ and $Ga_{21}Rh_4$ show practically the same Rh 3d binding energy that agrees well with the XPS measurements. However, XPS measurements on specially prepared intermetallic phases, presented in the next Chapter, show that 307.6 eV also perfectly matches the binding energy of the thermodynamic expected phase Ga_9Rh_2. Due to the higher resolution of synchrotron-based XPS, the Ga 3d region now shows a spin-orbit-split doublet that was fitted using two asymmetric signals. Regarding the lineshape and observed binding energy of 18.4 eV for the Ga $3d_{5/2}$ component, it can not be distinguished from metallic Ga. After exposure to air (Figure 13a and b, bottom), the recorded Rh 3d peaks widen slightly. The observed signal envelope is well reproduced by adding additional components (blue lines) shifted +0.4 eV to higher binding energy (308.0 eV for Rh $3d_{5/2}$). These additional components match the previously observed 308.0 eV components in the spectra of the oxidized macroscopic GaRh alloys (last Chapter, Figure 11, red component in the green and red spectra). Binding energies determined from DFT calculations show excellent agreement for Rh incorporated into the octahedral sites of the Ga_2O_3 lattice. For additional details the reader is referred to P1 and the dissertation of Sven Maisel[93]. Furthermore, the incorporation of Rh into the forming Ga_2O_3 is further confirmed by high-resolution, spatially-resolved EDX recorded of the Ga_2O_3 shell around GaRh particles in TEM studies, where an increased Rh content in the oxide shell is found (P2). In the Ga 3d region, the typical components expected for the formation of Ga_2O_3, Ga^{+3} signals at +2 eV, are seen. Due to the very high resolution of the measurements, two additional components at +1 eV to higher binding energies from the metallic Ga 3d components are necessary to reproduce the signal envelope. These components have been suggested in

literature and likely account for atoms at the Ga to Ga_2O_3 interface or substoichiometric Ga oxides.[48, 102]

A comparison to the oxidation of the macroscopic alloy systems presented in the last Chapter is possible when estimating the oxide film thickness from the ratio of oxidic/metallic Ga 3d components (Equation 11) and assuming a fully homogeneous system for the quantification. Quantification results for the Rh 3d component assigned to Rh incorporated into Ga_2O_3 compared to the estimated Ga_2O_3 film thickness agree well with the trends observed for the macroscopic alloys, Figure 14. Noteworthy is the surprisingly low Ga_2O_3 film thickness of slightly below 1 nm. Though the particle morphology was neglected for the quantification, the results for Rh incorporation in the investigated nano-system falls in the same order of magnitude as the macroscopic system. This supports that the knowledge-transfer is in principle possible.

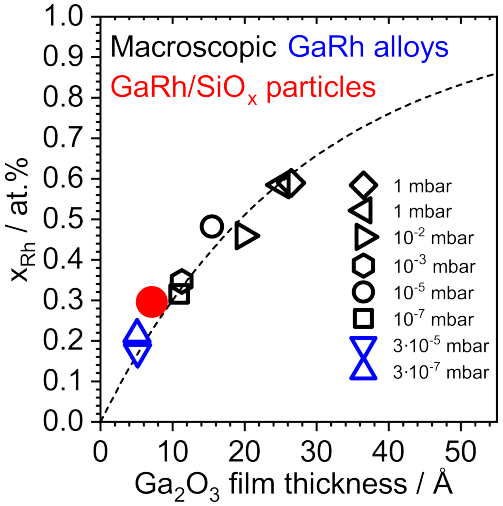

Figure 14 Shown is the development of the detected Rh content with the Ga_2O_3 film thickness as was already shown in Figure 10c in the last Chapter. Here, additionally the content of Rh incorporated into the Ga_2O_3 shell of the oxidized GaRh nano-systems is shown in red. (Adapted and modified from [50] with permission from AIP Publishing.)

In situ CO adsorption studies on GaPt/HOPG particles (P6)

Besides investigating the interaction with molecular oxygen, GaPt particles on HOPG as a flat model support were used for the first CO adsorption studies monitored by XPS for a SCALMS-like model system. These studies were performed at the HIPPIE beamline at MAX IV in Sweden, which allows for recording ambient pressure XPS and PM-IRAS simultaneously. GaPt particles were prepared by physical vapor deposition of 22.6 Å

Ga followed by 12.8 Å Pt (total of 42.4 at.% Pt in Ga), on a Ar^+ sputtered HOPG crystal. HOPG serves as a flat model support that provides certain advantages for the conducted experiment: The infrared reflectivity is good enough and it almost perfectly obeys metal surface selection rules, so that high quality IRAS spectra can be recorded in reflection geometry.[103] At the same time, HOPG does not alloy with Ga, in contrast to most metals. The interaction of HOPG with metallic particles is so week that Ar^+ sputtering is necessary to create defects to allow for nucleation of the deposited metal particles.[104, 105, 106, 107] Carbon monoxide was used as a probe molecule, since it is expected to strongly interact with the Pt centers. The combined IRAS and XPS approach provides simultaneous information on the binding strength and chemical state, while also allowing for a quantification of the adsorption sites. Results for CO adsorption on Pt/HOPG show that the system is well suited for such experiments.[72]

XPS measurements of the C 1s, Pt 4f and Ga 3d regions after preparation show clear indications of alloying based on the Pt 4f and Ga 3d binding energies. After the system was exposed to CO at room temperature, a small additional component in the C 1s region is found. Simultaneously, the IRAS spectrum suggests CO adsorption. With the exposure to CO, additional Ga 3d components appear that suggest the formation of Ga suboxides, likely due to impurities in the CO or displacements of H_2O form the chamber walls. After heating the particle system to 373 K, both the CO signals observed in XPS and IRAS disappear and can not be recovered when going to lower temperatures. This is ascribed to changes in the particles morphology (coalescence) that were also observed in *ex situ* atomic force microscopy. Additionally, the blocking of Pt adsorption sites by Ga oxide may play a role.

The near-ambient pressure XPS studies provided in P6 show initial proof that adsorption studies on SCALMS model particles are possible. Special attention needs, however, to be paid to the purity of the used gases due to the extreme oxophilicity of Ga.

4.4 XPS studies on GaRh intermetallic phases (P1, P4, P5)

The precipitation of intermetallic phases and the general phase behavior of the Ga-transition metal alloys have been a recurring, important topic in SCALMS research. While for the GaPd[91] and GaPt[108] systems, the binary phase diagrams are well studied, for the GaRh system only parts of the phase diagram are known.[109, 110] From our first results on the GaRh SCALMS system (P5), we expect that GaRh intermetallic phases in general are very interesting candidates for dehydrogenation catalysis. Extensive work on GaPd intermetallic phases has been published, where it was found that such intermetallic phases show good catalytic properties, e.g. for semihydration reactions or methanol steam reforming.[101, 111, 112, 113] It was shown that they can provide isolated transition metal sites at their surfaces[114] and that their electronic structures are significantly changed form the pure metal systems.[99] We expect similar catalytically interesting properties for GaRh intermetallic phases.

The investigation of the catalytic properties of the RhGa system urgently requires experimentally accessible reference materials, both for the comparison of spectroscopic results as well as for catalytic studies. We therefore aimed to synthesize two known GaRh intermetallic phases with low Rh concentration, Ga_9Rh_2 and Ga_3Rh.

For the preparation, a high vacuum (HV) oven at the chair of Kristallographie und Strukturphysik (Prof. Unruh) at FAU was used. This allows to fully melt the materials without excessive oxidation of Ga. Stiochiometric amounts of pure Ga and Rh were weighed into Al_2O_3 crucibles in air, placed into the oven and pumped to HV. After reaching 10^{-5} mbar, the samples were heated to 1000°C for 10 min to ensure that they are fully liquid. The phase diagram suggests liquidus temperatures around 740°C for Ga_9Rh_2 and around 950°C for Ga_3Rh. After keeping the alloys at 1000°C for 10 min, they were cooled to 500°C over 10 h and then kept at 500°C for another 10 h before cooling to room temperature.

The synthetic approach was used to form two polycrystalline ingots shown in Figure 15a and c. In addition, renderings of the crystal structure are shown, in 15b and 15d. X-ray diffraction and EDX studies confirm the Ga_9Rh_2 structure for our sample with 2:9 stoichiometry. For the 1:3 stochiometry, however, a new structure is found. The Ga_3Rh crystal structure was solved showing a new structure type with spacegroup $Cmc2_1$, which is unknown for this stoichiometry. Both the crystal structures for Ga_2Rh_9 and the new Ga_3Rh structure are build up from $RhGa_9$ units, in which Rh is surrounded by only Ga as next neighbors.

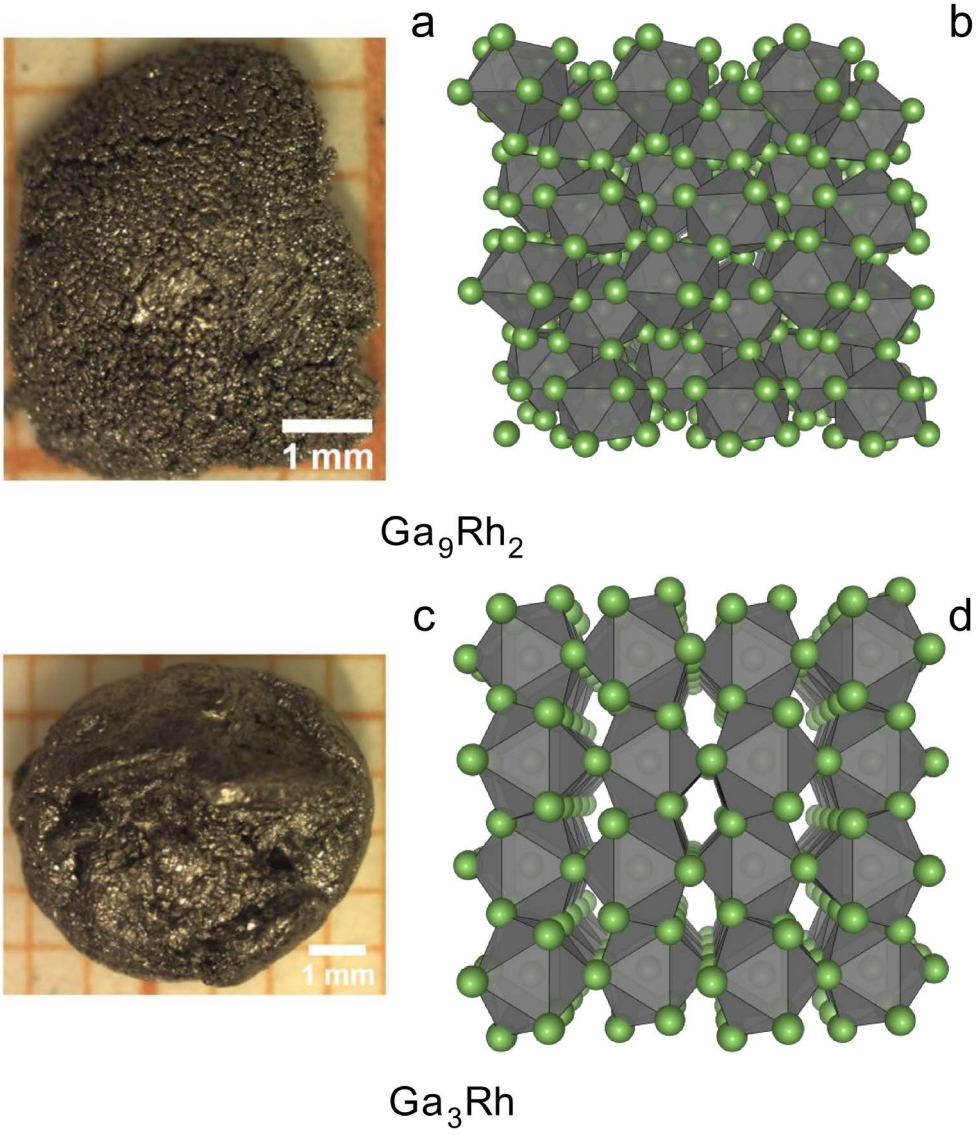

Figure 15 Ingots (a, c) and crystal structures (b, d) for Ga_2Rh_9 (top) and Ga_3Rh (bottom). Visual inspection and visible-light microscopy already show that the ingots are polycrystalline, with relatively small crystal facets. X-ray diffraction confirms the Ga_9Rh_2 structure known from literature (b). For Ga_3Rh a new structure was found and solved (d). (Atomic coordinates provided by Matthias Weißer)

DFT calculations showed that the low indexed surfaces of these crystals show well separated Rh atoms with distances above 4.7 Å, with exception of the (001) surface of Ga_3Rh where Rh-Rh distances of 3.28 Å were found. If such surfaces are stable under reaction conditions, the site isolation should be highly favorable for catalyzing dehydrogenation reactions. For additional details the reader is referred to P4.

After preparation, the samples were transported in air. A decomposition of the intermetallic surface in air is expected, similar to what was observed for GaPd intermetallic phases.[101, 112, 113] XPS measurements of the samples after transport show that the surface is covered by Ga_2O_3. It was however possible to remove most of the Ga_2O_3 by heating the samples in UHV to 600°C for 10 min. Figure 16 shows high resolution XPS measurements of both samples after heat treatment.

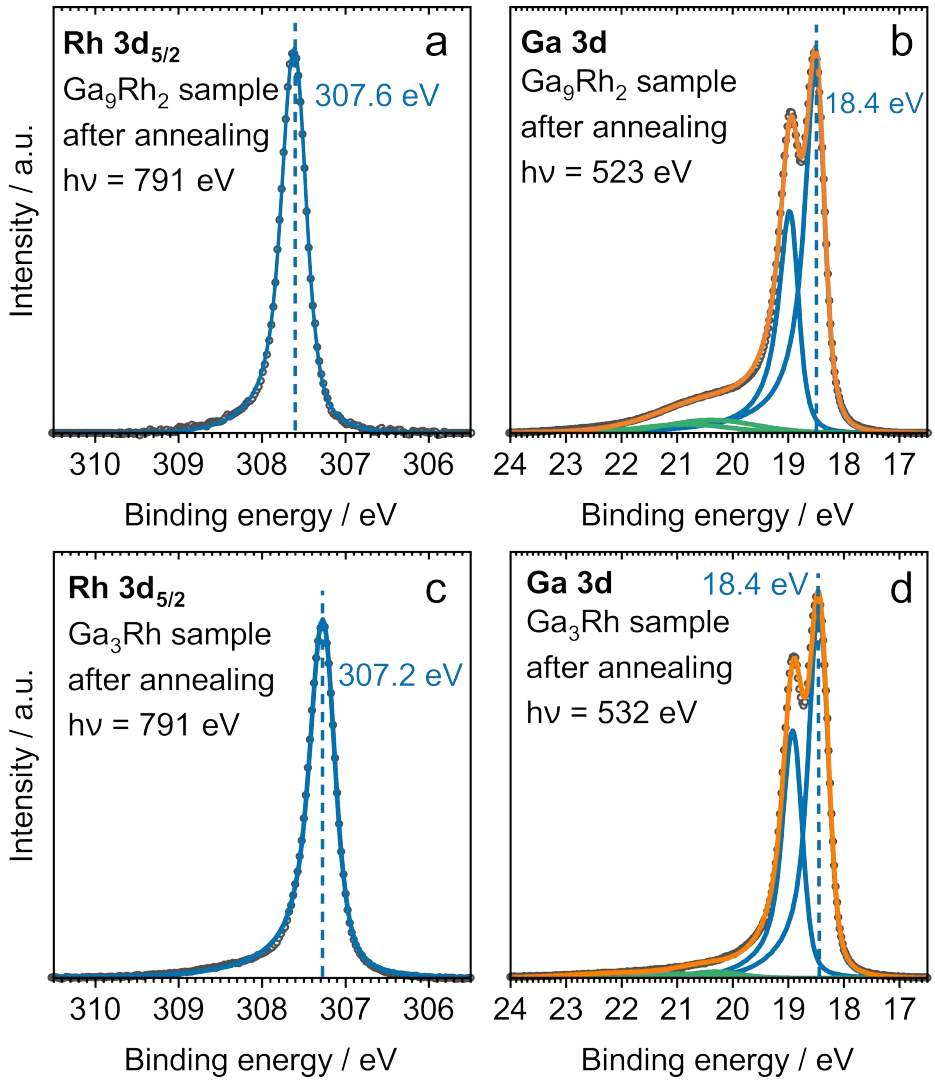

Figure 16 High-resolution synchrotron XP spectra of the Ga_9Rh_2 (a, b) and Ga_3Rh (c, d) samples after heat treatment at 600°C for 10 min in UHV. Both Ga 3d signals mostly resemble those of metallic Ga. Interesting are the unique binding energies of the Rh $3d_{5/2}$ components.

The Rh $3d_{5/2}$ binding energy detected for Ga_9Rh_2 is 307.6 eV, Ga $3d_{5/2}$ is 18.4 eV. These are the same binding energies that were previously observed for intermetallic phases crystallized on the macroscopic GaRh alloy and also for the SiO_2 supported GaRh model particle system. Both these systems were in a range of the phase diagram, where the formation Ga_9Rh_2 is expected, thus this result agrees with the so far presented measurements. DFT calculations match these measurements very well, what further supports that the measured binding energies actually result from Ga_9Rh_2. However, the quantification of the XPS data in Figure 16a, b shows a Rh content of 7 at.%, which is significantly lower than the expected value of around 18 at.%. This is most likely explained by remains of slightly overstoichiometric amounts of Ga used in the preparation. For the Ga_3Rh sample a Rh $3d_{5/2}$ binding energy of 307.2 eV is observed, while Ga $3d_{5/2}$ remains at 18.4 eV. This Rh 3d binding energy was not observed in any of the so far presented experiments. Again, binding energy shifts calculated by DFT agree nicely with the measured binding energies. For this sample, XPS quantification based on the shown deconvolution yields 23 at.% Rh, which agrees with the expected stoichiometry (25 at.% Rh). Notice that for both intermetallic phases the lineshapes are rather symmetric, in contrast to the lineshapes of pure Rh that are significantly more asymmetric. This asymmetry is rooted in valence band properties.[115]

Figure 17 shows measured valence band photoemission spectra (black) combined with valence bands (density of states) calculated by DFT (orange, by Sven Maisel). For Rh(111) (Figure 17a), the valence band spectrum is broad with an almost constant intensity starting from the valence band edge (0 eV) to a small maximum at 2.7 eV, after which the intensity decreases. Due to the large density of states close to E_F, the core level photo-excitation processes can "couple" well to the excitation of valence band electrons, which results in the asymmetry observed in XPS signals.[77, 42] In contrast, both the valence band spectra of Ga_3Rh (Figure 17b) and Ga_9Rh_2 (Figure 17c) show distinct maxima in intensity shifted by around 3.0 eV for Ga_3Rh and about 3.3 eV for Ga_9Rh_2 below the valence band edge. The more distinct maxima result in a reduced density of states at the valence band edge, which explains the more symmetric XPS signals. Density of states from DFT calculations support the measured valence band structures. Partial DOS calculations suggest that the distinct maxima observed for Ga_3Rh and Ga_9Rh_2 are mostly due to Rh 4d states. The changes in the valence bands were also shown to influence the observed XPS binding energies. DFT calculations reveal a complicated interplay between initial-state and final-state effects that result in the observed binding energy shifts, as stated in the end

of Chapter 2.2. The electronegativity difference between Ga and Rh results in an electron transfer to Rh. Nevertheless, a change of the screening of the generated "core hole", results in a shift to higher binding energy compared to pure Rh. The observed changes in the valence band significantly influence how the system reacts to a formed "core hole". For additional details the reader is referred to P4 and its supporting information.

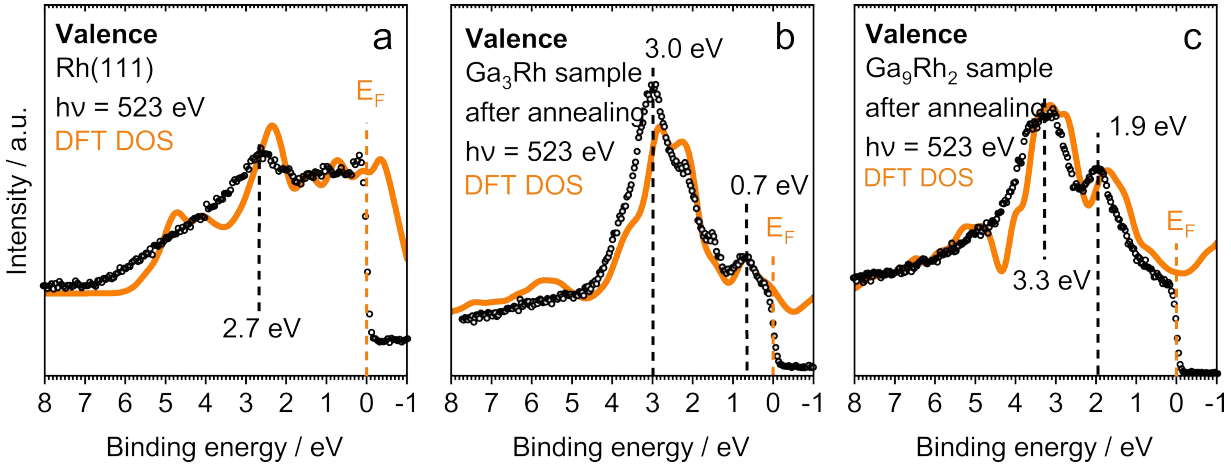

Figure 17 Measured valence band photoemission spectra (black) with DOSs calculated by DFT (orange, by Sven Maisel). In (a) for Rh(111), in (b) for Ga_3Rh and in (c) for Ga_9Rh_2. In all cases, there is good agreement between measurement and calculation. Note that the shown DFT density of states were not multiplied with an occupation function, the shown states are only occupied up to the Fermi energy E_F.

4.5 XPS studies on the binary GaIn system (P3)

High-temperature behavior of GaIn alloys:

The published research, including the so far introduced publications, investigated binary Ga-transition metal systems. For the material screening in search of promising catalysts so far, the transition metal was varied between Pd, Pt, Rh and more recently also Ni.[116] Especially interesting, also to further investigate the underlying mechanism of SCALMS, is the variation of the inert matrix material. The first obvious candidate is In, the addition of which can lead to a further decrease of the melting point. Elemental Ga has a melting temperature of 29.78°C, eutectic GaIn has a melting temperature of 15.3°C.[117] Potential ternary SCALMS systems like GaInPt are highly interesting to investigate and learn about the effects of the inert matrix material. A publication on the GaInPt system is in progress, while the herein introduced publication P3 is a XPS study on binary GaIn alloys. Especially relevant for catalysis is the first part of the publication, where the alloy surface is investigated in a temperature regime relevant for dehydrogenation catalysis (up to 800 K). The second part of P3 is a more general study of the phase transition behavior of GaIn.

Figure 18 shows a comparison of the relevant XP spectroscopic regions Ga 3d/In 4d, In 3d and Ga $2p_{3/2}$ of pure In (top), GaIn (mid) and pure Ga (bottom). The shown samples were measured at temperatures where the systems are fully liquid. The pure In reference was recorded at 600 K, pure Ga and GaIn were recorded at 400 K. Regarding the binding energy, for pure In the shown deconvolution yields an In $4d_{5/2}$ binding energy of 16.4 eV (Figure 18a, top) and 443.5 eV for In 3d (Figure 18b, top). For the pure Ga reference, the typical binding energies of Ga $3d_{5/2}$ and Ga $2p_{3/2}$ are 18.4 and 1116.7 eV respectively. For the roughly eutectic GaIn alloys the shown deconvolution suggests a slight shift of +0.35 eV to higher binding energy for the In components, for both In 4d and In 3d. The measured values mostly agree well with literature values, only the In 4d binding energy of pure In is typically reported at slightly higher binding energies.[48, 118, 119, 120, 121] Besides the binding energy shift, both In components narrow slightly due to the alloying. No changes in the binding energies of the Ga components are observed compared to the pure Ga alloy.

The shown fits were used for a quantitative analysis assuming a fully homogeneous alloy using sensitivity factors calculated from the measured pure elemental references. This quantification shows a significantly higher In content of around 22.1 at.%, according

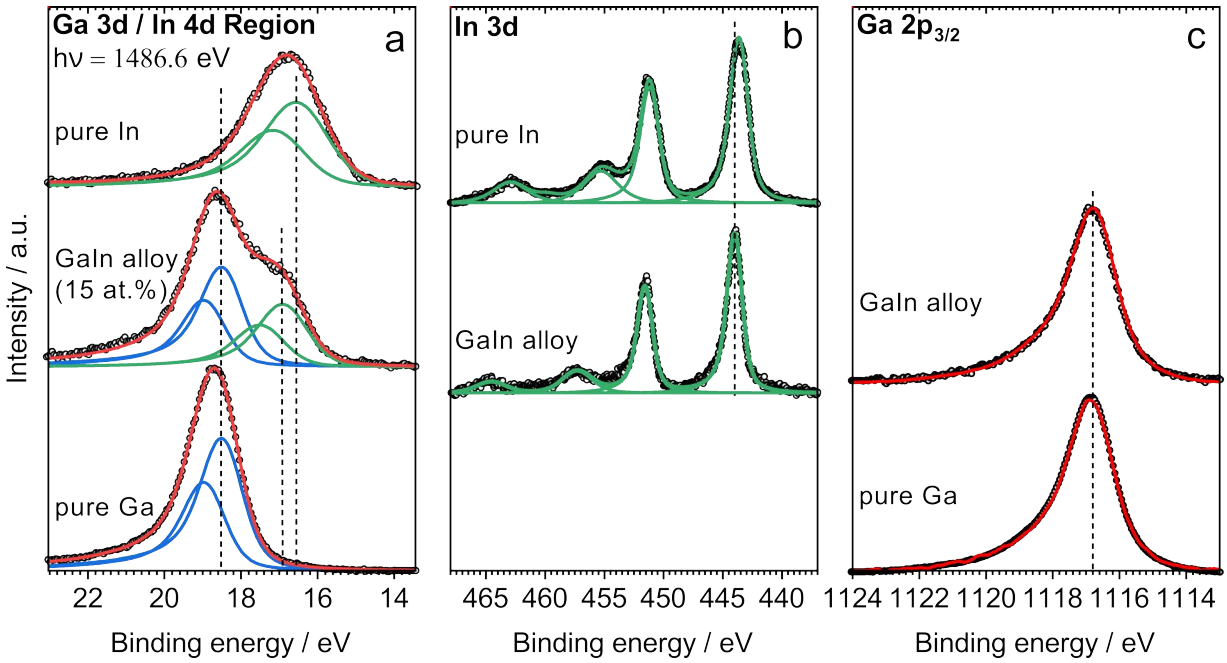

Figure 18 (a) Ga 3d/In 4d, (b) In 3d and (c) Ga $2p_{3/2}$ XP region of pure, liquid In, a roughly eutectic (15 at.% In in Ga) GaIn alloy and a liquid, pure Ga alloy. ((a) Adapted and modified from [35], copyright 2021 with permission by Elsevier.)

to Ga 3d/In 4d quantification, compared to the nominal In content according to weigh in of 15 at.%. Quantification using the more surface sensitive Ga $2p_{3/2}$ and In 3d core levels show an by even 2 at.% higher In content. This points to a surface segregation of In that results in an increased In content in the surface near region and the XPS interaction volume. Such an In surface segregation has been reported for GaIn alloys before.[122, 123, 124] Furthermore, In is reported to have lower surface free energy compared to Ga, therefore surface segregation is expected to be energetically favorable.[125]

To gain better insights into the liquid GaIn to vacuum interface, *ab initio* MD studies were performed by Sven Maisel for a slab system with a nearly eutectic bulk concentration for temperatures between 300 and 800 K. These simulations resulted in density profiles that show the Ga and In densities along the surface normal of the interface. As expected, the calculations show In surface enrichment. Interestingly, this enrichment seems to be confined to the first atomic layer. Furthermore, a temperature dependence was found, where with increasing temperature the In enrichment of the first atomic layer decreases slightly. Due to the computational costs of *ab initio* simulations, only relatively small systems (slab diameter around 30 Å) are used. An expected source of error is therefore the limited In atom reservoir. To ensure that these calculations reflect the real system, a

comparison to the spectroscopic data is necessary. To do so, the density profiles from the simulations are used to estimate overlayer systems from which XPS intensities are approximated. Figure 19 gives a size comparison of the slab model derived from the MD simulation (Figure 19a), the atom densities calculated from this layer model (Figure 19b), estimated atom densities (Figure 19c) and the information-depth of the relevant core levels (Figure 19d).

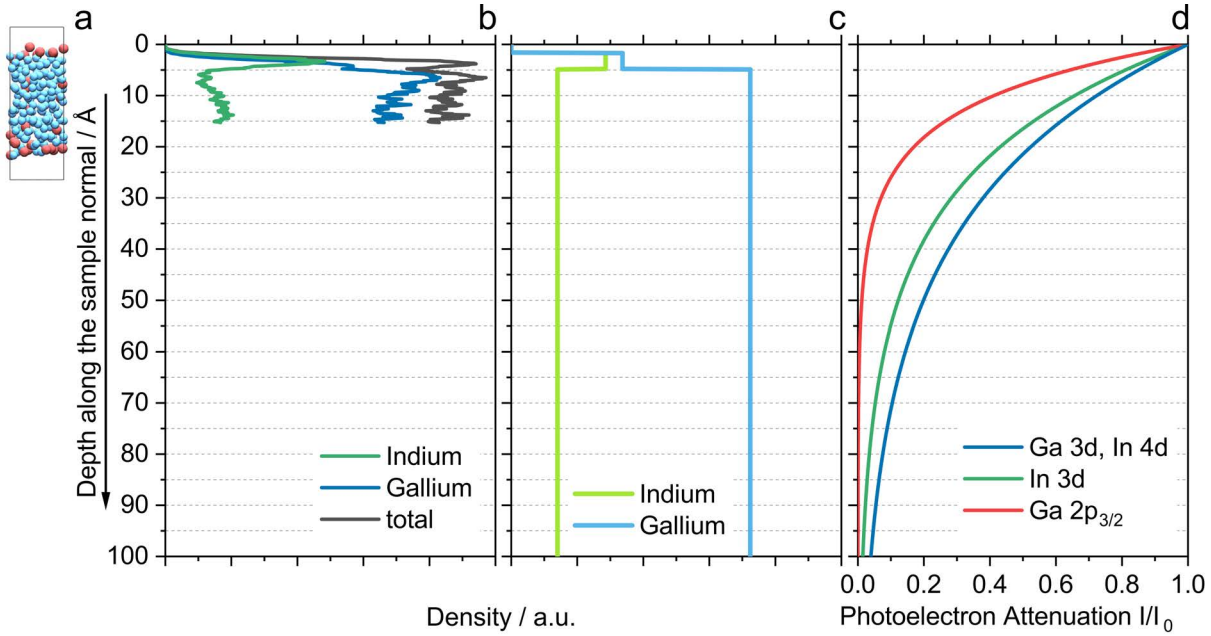

Figure 19 Size comparison of (a) *ab initio* MD slab, (b) the atom densities resulting form the *ab initio* MD, (c) the overlayer system used to estimate XPS intensities and (d) the information-depth of the relevant XPS core levels. The curves in (d) show what amount of the XPS peak intensity results from what depth for Al Kα excitation and normal emission geometry. The total signal intensity is the integral of the shown curves. *Ab initio* MD results (a, b) provided by Sven Maisel. (Adapted from the supporting information of [35], copyright 2021 with permission by Elsevier.)

A challenge when estimating intensities based on the MD calculation is the significantly larger information-depth (Figure 19d) compared to the slab-size (Figure 19a, b). To circumvent this mismatch in size, the bulk atom density used for XPS intensity approximation was extrapolated up to 100 Å. Equations 7 and 8 were used to estimate the

expected XPS intensities. For the constructed overlayer system (Figure 19c), the XPS intensity of e.g. Ga 3d is given by

$$I_{\mathrm{Ga\ 3d}} = \underbrace{\sigma_{\mathrm{Ga\ 3d}} T^{\mathrm{inst.}}_{\mathrm{Ga\ 3d}} J_{h\nu} n^{\mathrm{ol}}_{\mathrm{Ga}} \left(\lambda^{\mathrm{ol}}_{\mathrm{Ga\ 3d}} - \lambda^{\mathrm{ol}}_{\mathrm{Ga\ 3d}} \exp\left(-\frac{d_{\mathrm{ol}}}{\lambda^{\mathrm{ol}}_{\mathrm{Ga\ 3d}}} \right) \right)}_{\text{Surface contribution}} + \underbrace{\sigma_{\mathrm{Ga\ 3d}} T^{\mathrm{inst.}}_{\mathrm{Ga\ 3d}} J_{h\nu} n^{\mathrm{bulk}}_{\mathrm{Ga}} \lambda^{\mathrm{bulk}}_{\mathrm{Ga\ 3d}} \exp\left(-\frac{d_{\mathrm{ol}}}{\lambda^{\mathrm{ol}}_{\mathrm{Ga\ 3d}}} \right)}_{\text{Bulk contribution}} . \tag{12}$$

Intensities for other core levels are calculated in the same fashion.

To obtain more accurate values by canceling common errors, intensity ratios $\mathrm{I_{In\ 4d}/I_{Ga\ 3d}}$ and in P4 also $\mathrm{I_{In\ 3d}/I_{Ga\ 2p_{3/2}}}$, are formed. Figure 20 shows a comparison between experimental intensity ratios (black circles) and those calculated according to Equation 12 (blue squares). Additionally, the intensity ratio for a completely homogeneous alloy estimated according to Equation 6 as follows

$$\frac{I_{\mathrm{In\ 4d}}}{I_{\mathrm{Ga\ 3d}}} = \frac{\sigma_{\mathrm{In\ 4d}} T^{\mathrm{inst.}}_{\mathrm{In\ 4d}} n_{\mathrm{In}} \lambda_{\mathrm{In\ 4d}}}{\sigma_{\mathrm{Ga\ 3d}} T^{\mathrm{inst.}}_{\mathrm{Ga\ 3d}} n_{\mathrm{Ga}} \lambda_{\mathrm{Ga\ 3d}}}, \tag{13}$$

is shown as a red dashed line. The comparison with experimental data shows that the interface model based on the MD agrees much better compared to a homogeneous system. Both, the simulation and the experimental data, suggest a slight temperature dependence, since with increasing temperature, the In content is slightly reduced. Most likely this is a general effects due to the thermodynamics of the system: With higher temperature, entropic influences, counteracting the segregation, lead to a more homogeneous sample. Furthermore, increasing interatomic distances due to thermal expansion should also reduce the energy gain by the segregation of an element with lower surface free energy.

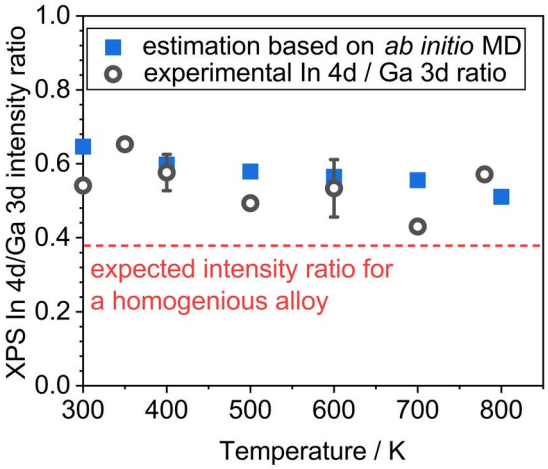

Figure 20 Comparison of the experimental $I_{In\ 4d}/I_{Ga\ 3d}$ intensity ratio (black circles) to intensity ratios estimated from the *ab initio* MD according to Equation 12 (blue squares). The dashed red line indicates the expected intensity ratio of a homogeneous eutectic alloy according to Equation 13. (Adapted from [35], copyright 2021 with permission by Elsevier.)

Low-temperature phase behavior of GaIn alloys:

In addition to the catalytically relevant temperature range, the low-temperature phase transition behavior of GaIn was investigated. To this end, cooling curves of hypoeutectic (In content >14.2 at.%) and hypereutectic (In content <14.2 at.%) GaIn alloys were recorded. Figure 21 shows the measured sample temperatures recorded during cooling for a hypoeutectic GaIn alloy with 3.5 at.% In (Figure 21a), and two hypereutectic GaIn alloys with 18 at.% In and 29 at.% In (Figure 21b). Cooling the liquid alloy results in an approximately exponential temperature decrease. In the shown hypoeutectic melt, the temperature decreases continuously down to 266 K, which is significantly below the melting temperature (supercooling). The decrease is followed by a temperature increase up to 292.6 K. This is interpreted as precipitation of solid Ga since the observed temperature matches the liquidus line of the GaIn phase diagram well.[117] The removal of Ga from the liquid results in the remaining melt becoming Ga lean, and thereby moving closer to the eutectic composition. This is reflected in a temperature decrease down to the melting temperature of eutectic GaIn 288.45 K, where the temperature remained constant for several minutes. The observed temperature development is interpreted as the solidification of the remaining melt.

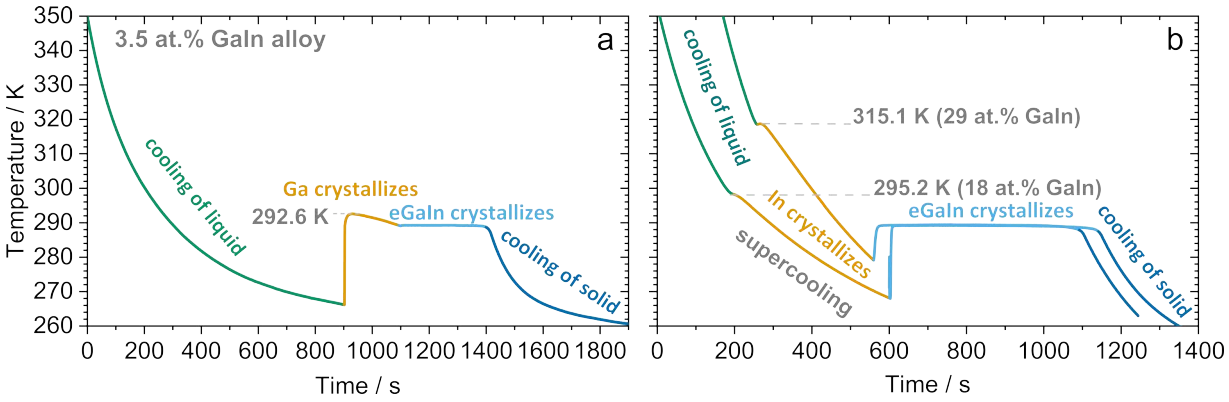

Figure 21 Cooling curves of a (a) hypoeutectic and (b) two hypereutectic GaIn alloys. The coloring shows the phase state of the measured alloy, that was assumed based on comparing the curve shape with the reported GaIn phase diagram.[117] For the hypoeutectic alloy, 292.6 K is the maximum temperature reached during Ga precipitation. For hypereutectic alloys, the indicated temperatures mark a kink in the temperature curve that indicates the beginning of In crystallization. (Adapted and modified from the supporting information of [35], copyright 2021 with permission by Elsevier.)

Once enough Ga is precipitated, the remaining melt reaches the eutectic composition (14.2 at.% In in Ga) and full solidification of the remaining melt occurs. Upon solidication the eutectic alloy segregates according to:

$$Ga_{85.8}In_{14.2}(l) \longrightarrow Ga(s) + Ga_{2.2}In_{97.8}(s)$$

Solidification is followed by a another, approximately exponential temperature decrease that is due to the cooling of the solid.

For the hypereutectic GaIn alloys, a well visible kink (green to orange part) in the cooling followed by a change in the slope of the temperature decay curve are observed. The temperatures of 315.1 K for 29 at.% In and 395.2 K for 18 at.% In match the points where the systems cross from their fully liquid states to their biphasic states according to the phase diagram.[117] Here, the precipitation of solid In is expected. The remaining melt thereby becomes more In-lean and the composition of the liquid moves closer to the eutectic composition. For both hypereutectic alloys supercooling is observed before the temperature increases close to the melting temperature of eutectic GaIn at 288.45 K. At this temperature, full solidification is expected to occur. Afterwards, another approximately exponential temperature decrease is measured, as the solid continues to cool down.

When comparing XP spectra recorded in the fully liquid state to those after solidification, significant differences are observed. Figure 22a shows that for a 18 at.% In, upon solidification, the In 4d signals (green) increase significantly, suggesting a further In enrichment at the surface. Simultaneously, the Ga 3d signals (blue) decrease. To obtain a

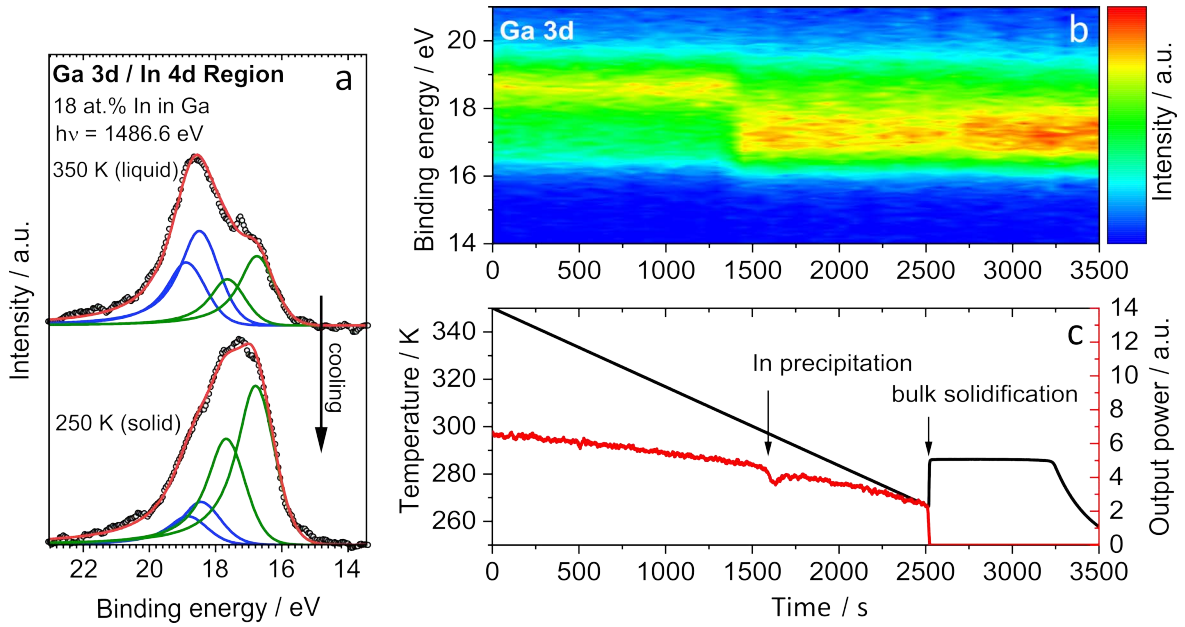

Figure 22 (a) Changes in the Ga 3d/In 4d region of a 18 at.% GaIn alloy observed when moving from a fully liquid system (top) to a fully solidified system (bottom). (b) Shows the time development of the Ga 3d/In 4d XP spectroscopic region during cooling. For comparison, (c) shows the time-resolved sample temperature (black) combined with the power output curve for sample heating. Approximately at the same time where the change in surface composition is observed in (b), a dip in heating power is observed in (c). This is attested to the heat of crystallization when In precipitates from the melt. (Adapted and modified from [35], copyright 2021 with permission by Elsevier.)

more detailed picture of the surface composition during cooling, time-dependent XPS of the Ga 3d/In 4d (Figure 22b), In 3d and Ga $2p_{3/2}$ regions was recorded during cooling. In order to slow down the cooling and thereby allow for more acquisition time, linear cooling ramps were programmed. In the linear cooling curve shown in Figure 22c, the transitions from the fully liquid to the biphasic state is visible as a dip in the power output of the voltage source (after approx. 1700 s). Here, due to the heat of crystallization, the power source does not need as much power output to maintain the linear cooling ramp against the liquid nitrogen heat sink. The later occurring bulk crystallization (after approx. 2500 s) still produces enough heat so that a large reminiscence feature

(temperature increase) is visible. Here, the power output completely drops because the temperature increases above the programmed cooling ramp. Additional density plots of the other spectroscopic regions are given in the publication (P3). In all monitored spectroscopic regions the change in surface composition occurs at the same time. Comparing the recorded spectra with the recorded heating power output shows that the change in the spectroscopic regions is observed slightly before the dip in heating power. The likely interpretation is that the already In-enriched surface acts as a starting point for In precipitation and that after precipitation at the surface, it continues in the bulk. This would explain the slight time delay between the observed changes in the XP regions and the drop in heating power. For further temperature-programmed XPS experiments on hypoeutectic alloys and additional hypereutectic alloys the reader is referred to P3.

All spectra recorded during cooling experiments were fitted using the fit models shown in Figure 22a. Pure element references were used to quantify the recorded spectra. While in the fully liquid states the quantification results between different experiments on the same sample agree reasonably well. In contrast, in the biphasic or solid state, the quantification results are highly scattered between experiments, see P3 for details. The likely explanation for the scatter between different solids obtained at the end of the cooling experiments is the micro structure of the forming alloy. Literature has shown that the micro structure can vary greatly. This can have a significant influence on the quantification results.[126, 127]

5 Summary

Catalysts with Ga-transition metal alloys supported on oxidic particles that were developed by the Wasserscheid group at FAU, and are referred to as supported catalytically active liquid metal solutions, SCALMS, have shown their capability to outperform industrial standard catalysts. Due to the low cost of liquid Ga compared to typical industrial catalysts, a future industrial application seems likely. From the start, XPS studies have been an integral part for developing an understanding of SCALMS catalysts. Temperature-dependent XPS studies on macroscopic Pd, Rh and Pt alloys have shown that the phase behavior of these alloys, in particular the precipitation of intermetallic phases, strongly influences the transition metal content in the surface near region. For the GaRh SCALMS system, the fully liquid state was shown to be associated with higher catalytic activity. Angle-resolved XPS studies combined with *ab initio* MD have led to the formulation of a hypothetical mechanism according to which catalytically active transition metal atoms dynamically appear at the otherwise transition metal depleted surface of the alloy.

The herein presented work discusses XPS investigation of Ga-based alloy systems in the context of SCALMS catalysis. This includes *in situ* oxidation studies on macroscopic GaRh and GaPd alloys, first studies on GaRh- and GaPt-supported particles, the synthesis and characterization of Ga_9Rh_2 and Ga_3Rh intermetallic phases, and XPS studies on the GaIn system with the aim of moving to ternary SCALMS. The presented results are expected to be of high relevance for the further development of SCALMS catalysis and, may also be valuable for other fields, where Ga alloys are applied.

Oxidation studies are highly relevant for any system containing Ga due to its high oxygen affinity. Even traces of molecular oxygen or water during catalyst synthesis, handling and technical application are likely to result in the formation of Ga oxides. The herein presented studies on the *in situ* oxidation of macroscopic GaRh and GaPd alloys build, and extend, on the oxidation studies on macroscopic GaPt and GaPd alloys presented by Grabau.[25, 32] The presented findings suggest that GaRh behaves similar to what was shown for GaPt: the exposure to molecular O_2 at 550 K results in the formation of a wetting Ga_2O_3 layer on the alloy. As a reaction to the formation of such oxide layers,

the transition metal redistributes to the surface and is incorporated into the forming Ga_2O_3. A closer analysis of the Rh 3d signal shows two different Rh 3d binding energies. This suggests that two effects contribute to the observed Rh surface enrichment. DFT studies show good agreement with the Rh 3d binding energies of, on the one hand, Rh rich intermetallic phases and, on the other hand, Rh atoms incorporated into the octahedral sites of the Ga_2O_3 crystal lattice. A likely explanation is that the forming liquid alloy / Ga_2O_3 interface presents a favorable nucleation site for GaRh intermetallics. The presence of molecular O_2 may lead to the decomposition of such intermetallics resulting in the formation of Ga_2O_3 and particles of intermetallic phases with lower Ga content. It is possible that such a decomposition also results in the incorporation of Rh atoms into Ga_2O_3.

In striking contrast to the GaRh system, the GaPd alloy shows no significant Pd incorporation into Ga_2O_3 when exposed to molecular O_2 at 550 K. During *in situ* oxidation, similarly, the formation of a wetting Ga_2O_3 layer is observed. Furthermore, also, a redistribution of Pd to the surface as a reaction to the Ga_2O_3 formation is seen, as is suggested by an initial increase of Pd 3d XPS intensity. However, after this inital increase, the observed Pd 3d signal decreases, very similar to the decrease of the metallic Ga signals. This suggests that the Ga_2O_3 film attenuates the Pd 3d photoelectrons, meaning that in contrast to Pt and Rh, Pd remains below the forming Ga_2O_3 film. *Ab initio* MD simulations support this interpretation, Pd atoms in a liquid Ga to Ga_2O_3 interface-slab model move to the Ga layer right below Ga_2O_3, suggesting that an enrichment below the interface is energetically favorable.

The *in situ* oxidation of macroscopic GaRh systems was taken further, by showing that the obtained results can be transferred to nano-alloy systems on flat SiO_2 model supports. Binding energies of high-resolution synchrotron XP spectra, and transmission electron microscopy similarly suggest that the formed nano-alloy particles are biphasic at room temperature, consisting of a mostly Rh-depleted Ga phase and Rh-rich GaRh intermetallic phases. After exposure to air, the formation of Ga_2O_3 was observed as expected, and additional components in the Rh 3d XPS regions hint at the incorporation of Rh into the formed Ga_2O_3. The observed XPS binding energies agree well with those measured for the macroscopic GaRh systems as well as with those that were calculated by DFT. In addition, spatially-resolved TEM EDX studies similarly show the Rh incorporation into Ga_2O_3. Overall, good agreement is found between the macroscopic alloys and the

supported nano-alloy systems. It was possible to explain all observed phenomena with knowledge gained from the macroscopic alloy systems.

GaPt particles on HOPG were investigated as a second SCALMS model system on a flat model support. The presented results demonstrate that combined IRAS and XPS studies for adsorbates on supported model GaPt particles are possible. It is to be expected, that with extensive optimization, these type of studies can yield highly relevant results for SCALMS catalysis.

From the beginning of SCALMS catalysis, the phase behavior and the various intermetallic phases present in the Ga-transition metal systems have been of high interest. Especially in the case of the GaRh system this presents a challenge due to the incomplete GaRh phase diagram. An additional motivation for the research on GaRh intermetallic phases is that from what is known about the dehydrogenation of short alkanes such as propane and butane, Ga-rich GaRh intermetallic phases should be good catalysts for the reaction. As Rh in these structures is fully coordinated by Ga, this likely results in surfaces with mostly isolated Rh sites, which should act as active sites with good coking resistance. In order to further investigate the electronic and catalytic properties of such systems, the intermetallic phases Ga_9Rh_2 and Ga_3Rh were prepared from stoichiometric amounts of the pure metals using a HV-capable oven. X-ray diffraction confirmed the successful preparation of Ga_9Rh_2, while for the Ga_3Rh intermetallic compound a so far unreported crystal structure with the 1:3 stoichiometry was found. First catalysis studies show promising catalytic properties for the two materials. Both intermetallic phases have been investigated by synchrotron XPS, including valence band measurements. Compared to the valence band of pure Rh(111), which is broad with an almost constant intensity over the first 3 eV, the valence bands of the two intermetallic phases show clear maxima of intensity that are shifted about 3 eV below the valence band edge. These measurements agree well with DFT-calculated density of states. The observed changes in the valence band are likely of high relevance for the catalytic properties. Though it is not the only deciding property, the energetic position of the d-band maximum is highly relevant for adsorption properties and catalytic reactivity.[128]

Besides their interesting catalytic properties, intermetallic phases may present model systems highly relevant for the investigation of SCALMS systems. The surfaces of Rh-lean GaRh intermetallic phases may allow for a characterization of the chemistry of Ga-coordinated Rh centers that should be similar to the proposed SCALMS-active site. In contrast to the SCALMS system, intermetallic surfaces are accessible for low-

temperature methods such as XPS adsorption studies with weakly adsorbing compounds. Furthermore, a comparison of the reactivities between intermetallic phases and SCALMS may allow one to single out the influence of the dynamic part of the proposed SCALMS mechanism on the catalytic properties.

A large part of the so far conducted research on SCALMS catalysis focused on the influence of changing the transition metal in the transition metal-Ga alloy. The presented work on the surface composition of the binary GaIn alloy lays the foundation for these studies. XPS studies on both the liquid and the solid GaIn system are presented. As was reported before, a significant In surface enrichment is found based on XPS quantification. This enrichment is temperature-dependent, that is, with increasing temperature the surface becomes less In enriched, an observation likely explained by the interplay of binding strength and mixing entropy. Since heterogeneous catalysis occurs at the outermost surface, this result is expected to be of high relevance for the coming catalytic studies on ternary GaInPt systems.

Apart form the catalytically relevant high-temperature behavior, temperature-dependent XPS studies at low temperature on the phase transition behavior of GaIn were presented. Upon solidification, a further In surface enrichment was observed both for the investigated hypereutectic and hypoeutectic alloys. It was found that the In enriched surface layer likely provides a nucleation point for In, so that once the systems transforms from the fully liquid, to the biphasic, and solid state, In further enriches at the surface. For both hypereuteic and hypoeutectic alloys, the observed segregation agrees well with the phase transitions reported in the bulk phase diagram. Noteworthy is a significant scatter in the observed degree of In enrichment for biphasic and solidified alloys. This is most likely attested to the microstructure of the forming solid. The results on the surface composition of GaIn alloys during solidification are of high relevance for low-temperature applications of these alloys.

6 Zusammenfassung

Flüssige Ga-Übergangsmetall-Legierungen auf oxidischen Trägerpartikeln (SCALMS) zeigen herausragende Eigenschaften für die katalytische Dehydrogenierung kurzkettiger Alkane. Das zugrundeliegende katalytische Konzept wurde von der Wasserscheid Gruppe an der FAU Erlangen-Nürnberg entwickelt. Einige der getesteten SCALMS-Katalysatoren übertreffen industrielle Standardkatalysatoren bereits ohne umfangreiche Optimierung. Aufgrund der geringen Kosten von Ga im Vergleich zu typischen Katalysatormaterialien scheint eine zukünftige industrielle Anwendung wahrscheinlich. XPS-Studien waren von Anfang an entscheidend für das Verständnis der Funktionsprinzipien von SCALMS. Temperaturabhängige XPS-Studien an makroskopischen Pd-, Rh- und Pt-Legierungen haben gezeigt, dass das Phasenverhalten dieser Legierungen, insbesondere das Auskristallisieren intermetallischer Phasen, den Übergangsmetallgehalt der oberflächennahen Region stark beeinflusst. Des weiteren wurde für GaRh-SCALMS eine höhere katalytische Aktivität für den vollständig flüssigen Zustand gezeigt. Basierend auf Winkel-aufgelösten XPS-Messungen in Kombination mit *ab initio* Molekulardynamik Rechnungen wurde als Mechanismus vorgeschlagen, dass katalytisch aktive Übergangsmetallatome dynamisch an der ansonsten an Übergangsmetall verarmten Oberfläche der Legierung erscheinen um die Dehydrogenierung zu katalysieren.

Die hier vorgestellten Studien befasst sich mit der weiteren XPS-Untersuchung von Ga-basierten Legierungen im Zusammenhang mit SCALMS-Katalyse. Dazu gehören *in situ* Oxidationsstudien an makroskopischen GaRh- und GaPd-Legierungen, erste Studien an geträgerten GaRh- und GaPt-Partikeln, die Synthese und Charakterisierung von intermetallischen Ga_9Rh_2- und Ga_3Rh-Phasen sowie XPS-Studien an binären GaIn-Legierungen mit dem Ziel diese als Matrixmaterial für ternären SCALMS zu nutzen. Es ist davon auszugehen, dass die vorgestellten Ergebnisse für die Weiterentwicklung des SCALMS-Konzept und auch für andere Bereiche, in denen Ga-Legierungen eingesetzt werden, von Nutzen sind.

Aufgrund der hohen Sauerstoffaffinität Galliums sind Oxidationsstudien von besonderer Bedeutung für Ga-basierte Katalysatoren. Selbst Spuren von molekularem Sauerstoff oder Wasser während der Katalysatorsynthese, der Handhabung und der technischen An-

wendung führen wahrscheinlich zur Bildung von Ga-Oxiden. Die hier vorgestellten Untersuchungen zur *in situ* Oxidation von makroskopischen GaRh- und GaPd-Legierungen bauen auf den von Grabau et al. vorgestellten Oxidationsexperimenten an makroskopischen GaPt- und GaPd-Legierungen auf und erweitern diese.[25, 32] GaRh zeigt ein ähnliches Verhalten wie GaPt: Molekularer Sauerstoff bei 550 K führt zur Bildung einer benetzenden Ga_2O_3-Schicht auf der Legierung. Als Reaktion auf die gebildete Oxidschichten reichert sich Rh an der Oberfläche der Legierung an und wird in das sich bildende Ga_2O_3 eingebaut. Eine genauere Analyse der Rh 3d Signale zeigt zwei unterschiedliche Bindungsenergien, was darauf hindeutet, dass zwei Effekte zu der beobachteten Rh Oberflächenanreicherung beitragen. DFT-Studien zeigen eine gute Übereinstimmung mit den Rh 3d Bindungsenergien von einerseits Rh-reichen intermetallischen Phasen und andererseits Rh-Atomen in den Oktaederlücken des Ga_2O_3-Kristallgitters. Eine wahrscheinliche Erklärung ist, dass die sich bildende Flüssiglegierung/Ga_2O_3-Grenzfläche die Bildung von GaRh intermetallischer Phasen begünstigt. Es ist zu erwarten, dass molekularer O_2 zur Zersetzung solcher Phasen unter Bildung von Ga_2O_3 und anderen GaRh-intermetallischen Phasen mit geringerem Ga-Gehalt führt. Möglicherweise führt eine derartige Reaktion auch zum Einbau von Rh-Atomen in das Ga_2O_3-Kristallgitter.

Während *in situ* Oxidationsstudien an GaPd-Legierungen wird ebenfalls die Bildung einer benetzenden Ga_2O_3-Schicht beobachtet. Darüber hinaus ist auch eine Umverteilung von Pd an die Oberfläche zu sehen, im auffälligem Gegensatz zum GaRh-System allerdings kein signifikanter Pd-Einbau in das sich bildende Ga_2O_3. Zwar kommt es während der Oxidation zu einem anfänglichen Anstieg der Pd 3d Intensität, nach kurzer Zeit nimmt das beobachtete Pd 3d-Signal jedoch ab. Die Intensitätsabnahme ähnelt vom Verlauf her dem der metallischen Ga-Signale, was darauf hindeutet, dass der auf der Oberfläche wachsende Ga_2O_3-Film die Pd 3d-Photoelektronen dämpft. Daraus wurde geschlossen, dass Pd im Gegensatz zu Pt und Rh unterhalb des sich bildenden Ga_2O_3-Films verbleibt. *Ab initio* MD-Simulationen stützen diese Interpretation: In einem Ga/Ga_2O_3-Grenzflächenmodell sind Positionen in der Ga-Atomlage direkt unterhalb des Oxides für Pd-Atome energetisch vorteilhaft.

Die Ergebnisse der *in situ* Oxidation von makroskopischen GaRh-Legierungen sind auf Nanolegierungen übertragbar. Für hochauflösendes Synchrotron-XPS wurde die native SiO_2-Schicht auf Si-Wafern als flaches Modellträgermaterial verwendet. Sowohl Bindungsenergien von hochauflösenden Synchrotron-XP-Spektren als auch Transmissionselektronenmikroskopie deuten darauf hin, dass die per physikalischer Gaspha-

senabscheidung hergestellten Nanolegierungen bei Raumtemperatur zweiphasig sind. Die Partikel bestehen überwiegend aus einer Rh-verarmten Ga-Phase und außerdem aus kristallinen, Rh-reichen intermetallischen GaRh-Phasen. Nachdem die Partikel Luft ausgesetzt wurden, wird wie erwartet die Bildung von Ga_2O_3 beobachtet. Zusätzliche Komponenten in den Rh 3d-XPS-Regionen deuten auf den Einbau von Rh in das gebildete Ga_2O_3 hin. Die beobachteten XPS-Bindungsenergien stimmen gut mit denen der makroskopischen GaRh-Legierungen und auch mit DFT berechneten Bindungsenergien überein. Darüber hinaus bestätigen auch ortsaufgelöste TEM-EDX Studien den Einbau von Rh in Ga_2O_3. Insgesamt ist also eine gute Übereinstimmung zwischen den makroskopischen Legierungen und den Nanolegierungssystemen festzustellen. Es war möglich, alle beobachteten Phänomene mit dem Wissen aus den makroskopischen Legierungssystemen zu erklären.

Neben den GaRh-Partikeln auf SiO_2 wurden GaPt-Partikel auf HOPG als zweites SCALMS-Modellsystem untersucht. Die vorgestellten Ergebnisse zeigen, dass kombinierte IRAS- und XPS-Studien für CO-Adsorption auf geträgerten GaPt-Nanolegierungen möglich sind. Es ist zu erwarten, dass diese Art von Studien bei weitgehender Optimierung hoch relevante Ergebnisse für die SCALMS-Katalyse liefern können.

Von Anfang an war das Phasenverhalten und die verschiedenen intermetallischen Phasen in den Ga-Übergangsmetallsystemen von großem Interesse für die Forschung an SCALMS Systemen. Insbesondere für das GaRh System stellt dies eine Herausforderung dar, weil das GaRh-Phasendiagramm nicht vollständig bekannt ist. Zusätzlich dazu sind, nach dem was über die Dehydrierung von kurzkettigen Alkanen bekannt ist, interessante katalytische Eigenschaften für GaRh-intermetallische Phasen zu erwarten. Rh-Atome sind in den Kristallgittern der intermetallischen Phasen $RhGa_3$ und Ga_9Rh_2 vollständig mit Ga koordiniert. Dies führt zu Oberflächen mit isolierten Rh-Zentren, von denen gute katalytische Aktivität mit gleichzeitiger Resistenz gegen Kohlenstoff-Ablagerung zu erwarten ist. Um die elektronischen und katalytischen Eigenschaften solcher Systeme weiter zu untersuchen, wurden die intermetallischen Phasen Ga_9Rh_2 und Ga_3Rh aus stöchiometrischen Mengen der reinen Metalle in einem HV-fähigen Ofen hergestellt. Röntgenbeugung bestätigte die Synthese von Ga_9Rh_2, während für die intermetallische Verbindung Ga_3Rh eine bisher nicht beschriebene Kristallstruktur gefunden wurde. Erste Katalysestudien zeigen vielversprechende katalytische Eigenschaften für beide Materialien. Beide intermetallische Phasen wurden mit Synchrotron-XPS untersucht, einschließlich Valenzbandmessungen. Im Vergleich zum breitem und in den ersten 3 eV

nahezu konstante Intensität aufweisenden Valenzband von reinem Rh(111), zeigen die Valenzbänder der beiden intermetallischen Phasen deutliche Intensitätsmaxima, die etwa 3 eV unter die Valenzbandkanten verschoben sind. Dies stimmt gut mit DFT-berechneten Zustandsdichten überein.

Neben den interessanten katalytischen Eigenschaften können intermetallische Phasen als Modellsysteme für die Untersuchung von SCALMS-Systemen wichtig seien. Die Oberflächen von Rh-armen GaRh-intermetallischen Phasen bieten einen Zugang zur Charakterisierung der Chemie von Ga-koordinierten Rh-Zentren. Im Gegensatz zum SCALMS-System sind die intermetallischen Oberflächen für Niedrigtemperaturmethoden wie XPS-Adsorptionsstudien mit schwach adsorbierenden Verbindungen zugänglich. Darüber hinaus könnte ein Vergleich der Reaktivitäten von intermetallischen Phasen und SCALMS dazu beitragen den Einfluss des flüssigen Aggregatzustandes von SCALMS auf die katalytischen Eigenschaften zu bestimmen.

Ein großer Teil der bisher durchgeführten Forschungsarbeit zur SCALMS-Katalyse konzentrierte sich auf den Einfluss verschiedener Übergangsmetalle in den Ga-Legierungen. Hier wurde nun der Einfluss eines weiteres p-Block Metall, Indium, untersucht. Es wurden XPS-Studien zur Oberflächenzusammensetzung binärer GaIn-Legierungen sowohl im flüssigen als auch im festen Zustand und während des Phasenübergangs vorgestellt. Die XPS-Quantifizierung zeigt eine erhebliche Anreicherung von In an der Oberfläche. Diese Anreicherung ist temperaturabhängig, d.h. mit steigender Temperatur sinkt der In-Gehalt der Oberfläche, eine Beobachtung, die wahrscheinlich durch das Zusammenspiel von Bindungsstärke und Mischungsentropie erklärt werden kann. Da die heterogene Katalyse an der äußersten Oberfläche stattfindet, dürfte dieses Ergebnis von großer Bedeutung für geplante katalytischen Untersuchungen an ternären GaInPt-Systemen sein.

Neben dem katalytisch relevanten Hochtemperaturverhalten wurden auch temperaturabhängige XPS-Studien bei niedriger Temperatur zum Phasenübergangsverhalten von GaIn vorgestellt. Nach der Erstarrung der Schmelze wurde eine weitere Anreicherung von In an der Oberfläche sowohl für hypereutektische als auch für hypoeutektische Legierungen beobachtet. Die In-angereicherte Oberflächenschicht dient wahrscheinlich als Keimbildungspunkt für In, so dass es zu einer weiteren In-Anreicherung kommt, sobald das System vom vollständig flüssigen in den biphasischen und festen Zustand übergeht. Sowohl bei hypereutektische als auch für hypoeutektische Legierungen stimmten die Temperaturen der beobachteten Entmischung gut mit den im Phasendiagramm überein.

Bemerkenswert ist eine erhebliche Streuung des gemessenen In-Gehalts bei zweiphasigen und erstarrten Legierungen. Dies ist höchstwahrscheinlich auf die Mikrostruktur des sich bildenden Festkörpers zurückzuführen. Es ist zu erwarten, dass die Oberflächenquantifizierungen und die Erkenntnisse über das Erstarrungsverhalten der GaIn-Legierungen von großer Bedeutung für Tieftemperaturanwendungen sind.

7 Bibliography

(1) Chen, S.; Chang, X.; Sun, G.; Zhang, T.; Xu, Y.; Wang, Y.; Pei, C.; Gong, J. *Chemical Society Reviews* **2021**, *50*, 3315–3354.

(2) Akah, A.; Al-Ghrami, M. *Applied Petrochemical Research* **2015**, *5*, 377–392.

(3) The Changing Landscape of Hydrocarbon Feedstocks for Chemical Production, `https://nap.nationalacademies.org/catalog/23555/the-changing-landscape-of-hydrocarbon-feedstocks-for-chemical-production-implications`, Accessed: 2022-03-12.

(4) Sattler, J. J. H. B.; Ruiz-Martinez, J.; Santillan-Jimenez, E.; Weckhuysen, B. M. *Chemical Reviews* **2014**, *114*, 10613–10653.

(5) Iglesias-Juez, A.; Beale, A. M.; Maaijen, K.; Weng, T. C.; Glatzel, P.; Weckhuysen, B. M. *Journal of Catalysis* **2010**, *276*, 268–279.

(6) Pham, H. N.; Sattler, J. J. H. B.; Weckhuysen, B. M.; Datye, A. K. *ACS Catalysis* **2016**, *6*, 2257–2264.

(7) Otroshchenko, T.; Sokolov, S.; Stoyanova, M.; Kondratenko, V. A.; Rodemerck, U.; Linke, D.; Kondratenko, E. V. *Angewandte Chemie International Edition* **2015**, *54*, 15880–15883.

(8) Taccardi, N.; Grabau, M.; Debuschewitz, J.; Distaso, M.; Brandl, M.; Hock, R.; Maier, F.; Papp, C.; Erhard, J.; Neiss, C.; Peukert, W.; Görling, A.; Steinrück, H.-P.; Wasserscheid, P. *Nature Chemistry* **2017**, *9*, 862–867.

(9) Görling, A.; Steinrück, H.-P.; Taccardi, N.; Wasserscheid, P.; Debuschewitz, J., Catalytically Active Compositions of Matter. Patent WO 2018036672 A1, 2018.

(10) Biloen, P.; Dautzenberg, F.; Sachtler, W. *Journal of Catalysis* **1977**, *50*, 77–86.

(11) Burton, J.; Hyman, E. *Journal of Catalysis* **1975**, *37*, 114–119.

(12) Hannagan, R. T.; Giannakakis, G.; Flytzani-Stephanopoulos, M.; Sykes, E. C. H. *Chemical Reviews* **2020**, *120*, 12044–12088.

(13) Sun, G.; Zhao, Z.-J.; Mu, R.; Zha, S.; Li, L.; Chen, S.; Zang, K.; Luo, J.; Li, Z.; Purdy, S. C.; Kropf, A. J.; Miller, J. T.; Zeng, L.; Gong, J. *Nature Communications* **2018**, *9*, 4454–4463.

(14) Nakaya, Y.; Hirayama, J.; Yamazoe, S.; Shimizu, K.; Furukawa, S. *Nature Communications* **2020**, *11*, 2838–2845.

(15) Hannagan, R. T.; Giannakakis, G.; Réocreux, R.; Schumann, J.; Finzel, J.; Wang, Y.; Michaelides, A.; Deshlahra, P.; Christopher, P.; Flytzani-Stephanopoulos, M.; Stamatakis, M.; Sykes, E. C. H. *Science* **2021**, *372*, 1444–1447.

(16) Zhou, J.; Xu, Z.; Xu, M.; Zhou, X.; Wu, K. *Nanoscale Advances* **2020**, *2*, 3624–3631.

(17) Liu, Y.; Li, Z.; Yu, Q.; Chen, Y.; Chai, Z.; Zhao, G.; Liu, S.; Cheong, W.-C.; Pan, Y.; Zhang, Q.; Gu, L.; Zheng, L.; Wang, Y.; Lu, Y.; Wang, D.; Chen, C.; Peng, Q.; Liu, Y.; Liu, L.; Chen, J.; Li, Y. *Journal of the American Chemical Society* **2019**, *141*, 9305–9311.

(18) Resasco, J.; Christopher, P. *The Journal of Physical Chemistry Letters* **2020**, *11*, 10114–10123.

(19) Daeneke, T.; Khoshmanesh, K.; Mahmood, N.; de Castro, I. A.; Esrafilzadeh, D.; Barrow, S. J.; Dickey, M. D.; Kalantar-zadeh, K. *Chemical Society Reviews* **2018**, *47*, 4073–4111.

(20) Zuraiqi, K.; Zavabeti, A.; Allioux, F.-M.; Tang, J.; Nguyen, C. K.; Tafazolymotie, P.; Mayyas, M.; Ramarao, A. V.; Spencer, M.; Shah, K.; McConville, C. F.; Kalantar-Zadeh, K.; Chiang, K.; Daeneke, T. *Joule* **2020**, *4*, 2290–2321.

(21) Upham, D. C.; Agarwal, V.; Khechfe, A.; Snodgrass, Z. R.; Gordon, M. J.; Metiu, H.; McFarland, E. W. *Science* **2017**, *358*, 917–921.

(22) Palmer, C.; Upham, D. C.; Smart, S.; Gordon, M. J.; Metiu, H.; McFarland, E. W. *Nature Catalysis* **2020**, *3*, 83–89.

(23) Liu, H.; Xia, J.; Zhang, N.; Cheng, H.; Bi, W.; Zu, X.; Chu, W.; Wu, H.; Wu, C.; Xie, Y. *Nature Catalysis* **2021**, *4*, 202–211.

(24) Grabau, M.; Erhard, J.; Taccardi, N.; Calderon, S. K.; Wasserscheid, P.; Görling, A.; Steinruck, H.-P.; Papp, C. *Chemistry - A European Journal* **2017**, *23*, 17701–17706.

(25) Grabau, M., X-ray Photoemission Studies of Bimetallic Pt-Ga, Pd-Ga and Rh-Ga Catalysts: Untersuchungen an Bimetallischen Pt-Ga, Pd-Ga und Rh-Ga Katalysatoren Mittels Röntgenphotoelektronenspektroskopie.
Dissertation thesis, Friedrich-Alexander-Universität Erlangen-Nürnberg, 2018.

(26) Raman, N.; Maisel, S.; Grabau, M.; Taccardi, N.; Debuschewitz, J.; Wolf, M.; Wittkämper, H.; Bauer, T.; Wu, M.; Haumann, M.; Papp, C.; Görling, A.; Spiecker, E.; Libuda, J.; Steinrück, H.-P.; Wasserscheid, P. *ACS Catalysis* **2019**, *9*, 9499–9507.

(27) Kettner, M.; Maisel, S.; Stumm, C.; Schwarz, M.; Schuschke, C.; Görling, A.; Libuda, J. *Journal of Catalysis* **2019**, *369*, 33–46.

(28) Hohner, C.; Kettner, M.; Stumm, C.; Schuschke, C.; Schwarz, M.; Libuda, J. *Topics in Catalysis* **2019**, *62*, 849–858.

(29) Hohner, C.; Kettner, M.; Stumm, C.; Blaumeiser, D.; Wittkämper, H.; Grabau, M.; Schwarz, M.; Schuschke, C.; Lykhach, Y.; Papp, C.; Steinrück, H.-P.; Libuda, J. *The Journal of Physical Chemistry C* **2020**, *124*, 2562–2573.

(30) Raman, N.; Wolf, M.; Heller, M.; Heene-Wurl, N.; Taccardi, N.; Haumann, M.; Felfer, P.; Wasserscheid, P. *ACS Catalysis* **2021**, *11*, 13423–13433.

(31) Bauer, T.; Maisel, S.; Blaumeiser, D.; Vecchietti, J.; Taccardi, N.; Wasserscheid, P.; Bonivardi, A.; Görling, A.; Libuda, J. *ACS Catalysis* **2019**, *9*, 2842–2853.

(32) Grabau, M.; Calderón, S. K.; Rietzler, F.; Niedermaier, I.; Taccardi, N.; Wasserscheid, P.; Maier, F.; Steinrück, H.-P.; Papp, C. *Surface Science* **2016**, *651*, 16–21.

(33) Imbihl, R.; Behm, R. J.; Schlögl, R. *Physical Chemistry Chemical Physics* **2007**, *9*, 3459.

(34) Editorial: Mind the gap. *Nature catalysis* **2018**, 1, 807-808.

(35) Wittkämper, H.; Maisel, S.; Moritz, M.; Grabau, M.; Görling, A.; Steinrück, H.-P.; Papp, C. *Surface Science* **2022**, *717*, 122008.

(36) Raman, N.; Maisel, S.; Grabau, M.; Taccardi, N.; Debuschewitz, J.; Wolf, M.; Wittkämper, H.; Bauer, T.; Wu, M.; Haumann, M.; Papp, C.; Görling, A.; Spiecker, E.; Libuda, J.; Steinrück, H.-P.; Wasserscheid, P. *ACS Catalysis* **2019**, *9*, 9499–9507.

(37) Hertz, H. *Annalen der Physik und Chemie* **1887**, *267*, 983–1000.

(38) Einstein, A. *Annalen der Physik* **1905**, *322*, 132–148.

(39) `https://www.nobelprize.org/prizes/physics/1921/einstein/facts/`, accessed: 2022-01-18.

(40) `https://www.nobelprize.org/prizes/physics/1981/siegbahn/facts/`, accessed: 2022-01-18.

(41) `https://www.nobelprize.org/uploads/2018/06/siegbahn-lecture-1.pdf`, accessed: 2022-01-18.

(42) Fadley, C. S., *Basic Concepts of X-ray Photoelectron Spectroscopy*, part of Electron Spectroscopy: Theory, Techniques and Applications by Brundle and Baker; Academic Press: 1977.

(43) Krause, M. O.; Ferreira, J. G. *Journal of Physics B: Atomic and Molecular Physics* **1975**, *8*, 2007–2014.

(44) Ibach, H.; Lüth, H., *Festkorperphysik*; Springer Berlin Heidelberg: 2009.

(45) Kinosnita, I.; Ishii, J. *International Journal of Thermophysics* **2011**, *32*, 1387–1398.

(46) Hüfner, S., *Photoelectron Spectroscopy*; Springer Berlin Heidelberg: 2003.

(47) Linford, M. *Vacuum Technology & Coating* **2014**, 25–31.

(48) Surdu-Bob, C.; Saied, S.; Sullivan, J. *Applied Surface Science* **2001**, *183*, 126–136.

(49) Riedel, E.; Meyer, H.-J., *Allgemeine und Anorganische Chemie*; De Gruyter: 2018.

(50) Wittkämper, H.; Maisel, S.; Wu, M.; Frisch, J.; Wilks, R. G.; Grabau, M.; Spiecker, E.; Bär, M.; Görling, A.; Steinrück, H.-P.; Papp, C. *The Journal of Chemical Physics* **2020**, *153*, 104702–104715.

(51) Wittkämper, H.; Maisel, S.; Moritz, M.; Grabau, M.; Görling, A.; Steinrück, H.-P.; Papp, C. *Physical Chemistry Chemical Physics* **2021**, *23*, 16324–16333.

(52) Seah, M. P. *Surface and Interface Analysis* **1980**, *2*, 222–239.

(53) Seah, M. P.; Anthony, M. T. *Surface and Interface Analysis* **1984**, *6*, 230–241.

(54) Scofield, J.H. *Office of Scientific and Technical Information (OSTI)* **1973**.

(55) Yeh, J.; Lindau, I. *Atomic Data and Nuclear Data Tables* **1985**, *32*, 1–155.

(56) Trzhaskovskaya, M.; Nefedov, V.; Yarzhemsky, V. *Atomic Data and Nuclear Data Tables* **2001**, *77*, 97–159.

(57) Trzhaskovskaya, M.; Nefedov, V.; Yarzhemsky, V. *Atomic Data and Nuclear Data Tables* **2002**, *82*, 257–311.

(58) Ruffieux, P.; Schwaller, P.; Groning, O.; Schlapbach, L.; Groning, P.; Herd, Q. C.; Funnemann, D.; Westermann, J. *Review of Scientific Instruments* **2000**, *71*, 3634.

(59) Tanuma, S.; Powell, C. J.; Penn, D. R. *Surface and Interface Analysis* **2003**, *35*, 268–275.

(60) Bethe, H.; Hund, F.; Mott, N. F.; Pauli, W.; Rubinowicz, A.; Wentzel, G.; Smekal, A., *Quantentheorie*; Springer Berlin Heidelberg: 1933.

(61) Cooper, J.; Zare, R. N. *The Journal of Chemical Physics* **1968**, *48*, 942–943.

(62) Cooper, J.; Zare, R. N. *The Journal of Chemical Physics* **1968**, *49*, 4252–4252.

(63) Cooper, J.; Zare, R. N., *Lectures in theoretical physics: Atomic collision processes*; Gordon and Breach: 1969.

(64) Manson, S. T.; Starace, A. F. *Reviews of Modern Physics* **1982**, *54*, 389–405.

(65) Pantförder, J., Photoelektronenspektroskopie im "Pressure Gap" - Aufbau einer neuen Apparatur fur Messungen im Druckbereich von 10^{-10} bis 1 mbar. Dissertation thesis, Friedrich-Alexander-Universität Erlangen-Nürnberg, 2005.

(66) Omicron NanoTechnology, EA 125 Energy Analyser User's Guide. **2002**, Version 2.1.

(67) Pantförder, J.; Pöllmann, S.; Zhu, J. F.; Borgmann, D.; Denecke, R.; Steinrück, H.-P. *Review of Scientific Instruments* **2005**, *76*, 014102.

(68) Wittkämper, H.; Hock, R.; Weisser, M.; Dallmann, J.; Vogel, C. S.; Raman, N.; Haumann, M.; Wasserscheid, P.; Hsieh, T.-E.; Maisel, S.; Moritz, M.; Wichmann, C.; Frisch, J.; Gorgoi, M.; Wilks, R. G.; Bär, M.; Wu, M.; Spiecker, E.; Görling, A.; Unruh, T.; Steinrück, H.-P.; Papp, C. *submitted* **2022**.

(69) `https://www.helmholtz-berlin.de/pubbin/igama_output?modus=einzel&sprache=en&gid=1983&typoid=75136`, accessed: 2022-02-23.

(70) Zhu, S.; Scardamaglia, M.; Kundsen, J.; Sankari, R.; Tarawneh, H.; Temperton, R.; Pickworth, L.; Cavalca, F.; Wang, C.; Tissot, H.; Weissenrieder, J.; Hagman, B.; Gustafson, J.; Kaya, S.; Lindgren, F.; Kallquist, I.; Maibach, J.; Hahlin, M.; Boix, V.; Gallo, T.; Rehman, F.; D'Acunto, G.; Schnadt, J.; Shavorskiy, A. *Journal of Synchrotron Radiation* **2021**, *28*, 624–636.

(71) Knudsen, J.; Andersen, J. N.; Schnadt, J. *Surface Science* **2016**, *646*, 160–169.

(72) Porsgaard, S.; Ono, L. K.; Zeuthen, H.; Knudsen, J.; Schnadt, J.; Merte, L. R.; Chevallier, J.; Helveg, S.; Salmeron, M.; Wendt, S.; Besenbacher, F. *ChemPhysChem* **2013**, *14*, 1553–1557.

(73) CasaXPS Manual 2.3.15, `http://www.casaxps.com/ebooks/OrangeBookRev1.3ebook.pdf`, Accessed: 2022-02-23.

(74) Evans, S. *Surface and Interface Analysis* **1991**, *17*, 85–93.

(75) Synthetic peak line-shapes, http://www.casaxps.com/help_manual/line_shapes.htm, Accessed: 2022-02-23.

(76) Cardona, M.; Ley, L., *Photoemission in Solids I*; Springer Berlin Heidelberg: 1978.

(77) Doniach, S.; Sunjic, M. *Journal of Physics C: Solid State Physics* **1970**, *3*, 285–291.

(78) Major, G.; Shah, D.; Fernandez, V.; Fairley, N.; Linford, M. *Vacuum Technology & Coating* **2020**.

(79) Major, G.; Shah, D.; Avval, T.; Fernandez, V.; Fairley, N.; Linford, M. *Vacuum Technology & Coating* **2020**.

(80) Lorentzian Asymmetric Lineshape, http://www.casaxps.com/help_manual/manual_updates/LA_Lineshape.pdf, accessed: 2022-02-23.

(81) Brauer, G., *Handbuch der praparativen anorganischen Chemie 3., umgearbeitete Auflage Band I*; Enke: Stuttgart.

(82) Carli, R.; Bianchi, C. *Applied Surface Science* **1994**, *74*, 99–102.

(83) Chabala, J. M. *Physical Review B* **1992**, *46*, 11346–11357.

(84) Grabau, M.; Steinrück, H.-P.; Papp, C. *Surface Science* **2018**, *677*, 254–257.

(85) Niemantsverdriet, J. W., *Spectroscopy in Catalysis*; Wiley: 2007.

(86) Kibis, L. S.; Stadnichenko, A. I.; Koscheev, S. V.; Zaikovskii, V. I.; Boronin, A. I. *The Journal of Physical Chemistry C* **2016**, *120*, 19142–19150.

(87) Moulder, J.; Chastain, J., *Handbook of X-ray Photoelectron Spectroscopy: A Reference Book of Standard Spectra for Identification and Interpretation of XPS Data*; Physical Electronics Division, Perkin-Elmer Corporation: 1992.

(88) Wittkamper, H.; Maisel, S.; Wu, M.; Frisch, J.; Wilks, R. G.; Grabau, M.; Spiecker, E.; Bar, M.; Gorling, A.; Steinruck, H.-P.; Papp, C. *The Journal of Chemical Physics* **2020**, *153*, 104702.

(89) Jeurgens, L.; Sloof, W.; Tichelaar, F.; Mittemeijer, E. *Surface Science* **2002**, *506*, 313–332.

(90) Mårtensson, N.; Nyholm, R.; Johansson, B. *Physical Review Letters* **1980**, *45*, 754–757.

(91) Okamoto, H. *Journal of Phase Equilibria and Diffusion* **2008**, *29*, 466–467.

(92) T.B., M., *Binary alloy phase diagrams. V. 2*; Materials Park, Ohio: ASM International: 1990.

(93) Maisel, S., Investigation of Novel Liquid Metal Catalysts with Density-Functional Methods. Dissertation thesis, Friedrich-Alexander-Universität Erlangen-Nürnberg, 2021.

(94) Qi, W. *Accounts of Chemical Research* **2016**, *49*, 1587–1595.

(95) Baraldi, A.; Lizzit, S.; Novello, A.; Comelli, G.; Rosei, R. *Physical Review B* **2003**, *67*, 205404–205410.

(96) Andersen, J. N.; Hennig, D.; Lundgren, E.; Methfessel, M.; Nyholm, R.; Scheffler, M. *Physical Review B* **1994**, *50*, 17525–17533.

(97) Ganduglia-Pirovano, M. V.; Scheffler, M.; Baraldi, A.; Lizzit, S.; Comelli, G.; Paolucci, G.; Rosei, R. *Physical Review B* **2001**, *63*, 205415–205426.

(98) Lindner, U.; Papp, H. *Fresenius Journal of Analytical Chemistry* **1991**, *341*, 387–394.

(99) Kovnir, K., Teschner, D., Armbruster, M., Schnorch, P., Havecker, M., Knop-Gericke, A., et al. (2008). Pinning the catalytic centre: A new concept for catalysts development. In K. Godehusen (Ed.), BESSY Highlights 2007 (pp. 22-23). Berlin: Berliner Elektronenspeicherring-Gesellschaft für Synchrotronstrahlung m.b.H. (BESSY).

(100) Kovnir, K.; Armbrüster, M.; Teschner, D.; Venkov, T.; Jentoft, F.; Knop-Gericke, A.; Grin, Y.; Schlögl, R. *Science and Technology of Advanced Materials* **2007**, *8*, 420–427.

(101) Wowsnick, G.; Teschner, D.; Kasatkin, I.; Girgsdies, F.; Armbrüster, M.; Zhang, A.; Grin, Y.; Schlögl, R.; Behrens, M. *Journal of Catalysis* **2014**, *309*, 209–220.

(102) Su, C. Y.; Skeath, P. R.; Lindau, I.; Spicer, W. E. *Surface Science* **1982**, *118*, 248–256.

(103) Heidberg, J.; Warskulat, M.; Folman, M. *Journal of Electron Spectroscopy and Related Phenomena* **1990**, *54-55*, 961–970.

(104) Favaro, M.; Agnoli, S.; Perini, L.; Durante, C.; Gennaro, A.; Granozzi, G. *Physical Chemistry Chemical Physics* **2013**, *15*, 2923–2931.

(105) Kettner, M.; Stumm, C.; Schwarz, M.; Schuschke, C.; Libuda, J. *Surface Science* **2019**, *679*, 64–73.

(106) Yang, D.-Q.; Sacher, E. *Surface Science* **2002**, *516*, 43–55.

(107) Bukhtiyarov, A. V.; Prosvirin, I. P.; Bukhtiyarov, V. I. *Applied Surface Science* **2016**, *367*, 214–221.

(108) Li, M.; Li, C.; Wang, F.; Zhang, W. *Intermetallics* **2006**, *14*, 826–831.

(109) Anres, P.; Gaune-Escard, M.; Bros, J. P. *Journal of Alloys and Compounds* **1998**, *265*, 201–208.

(110) Anres, P.; Gaune-Escard, M.; Bross, J. P. *Journal of Phase Equilibria* **1997**, *18*, 417–417.

(111) Iwasa, N.; Mayanagi, T.; Ogawa, N.; Sakata, K.; Takezawa, N. *Catalysis Letters* **1998**, *54*, 119–123.

(112) Haghofer, A.; Föttinger, K.; Girgsdies, F.; Teschner, D.; Knop-Gericke, A.; Schlögl, R.; Rupprechter, G. *Journal of Catalysis* **2012**, *286*, 13–21.

(113) Wowsnick, G.; Teschner, D.; Armbrüster, M.; Kasatkin, I.; Girgsdies, F.; Grin, Y.; Schlögl, R.; Behrens, M. *Journal of Catalysis* **2014**, *309*, 221–230.

(114) Prinz, J.; Gaspari, R.; Pignedoli, C. A.; Vogt, J.; Gille, P.; Armbrüster, M.; Brune, H.; Gröning, O.; Passerone, D.; Widmer, R. *Angewandte Chemie International Edition* **2012**, *51*, 9339–9343.

(115) O'Connor, C. R.; van Spronsen, M. A.; Karatok, M.; Boscoboinik, J.; Friend, C. M.; Montemore, M. M. *The Journal of Physical Chemistry C* **2021**, *125*, 10685–10692.

(116) Søgaard, A.; de Oliveira, A. L.; Taccardi, N.; Haumann, M.; Wasserscheid, P. *Catalysis Science & Technology* **2021**, *11*, 7535–7539.

(117) Anderson, T.; Ansara, I. *Journal of Phase Equilibria* **1991**, *12*, 64–72.

(118) Maira, G. K.; Orton, B. R.; Riviere, J. C. *Journal of Physics F: Metal Physics* **1987**, *17*, 1999–2006.

(119) Nyholm, R.; Mårtensson, N. *Solid State Communications* **1981**, *40*, 311–314.

(120) Pessa, M.; Vuoristo, A.; Vulli, M.; Aksela, S.; Väyrynen, J.; Rantala, T.; Aksela, H. *Physical Review B* **1979**, *20*, 3115–3123.

(121) Fuggle, J. C.; Mårtensson, N. *Journal of Electron Spectroscopy and Related Phenomena* **1980**, *21*, 275–281.

(122) Hubbard, K. M.; Weller, R. A.; Weathers, D. L.; Tombrello, T. *Nuclear Instruments and Methods in Physics Research Section B: Beam Interactions with Materials and Atoms* **1989**, *36*, 395–403.

(123) Regan, M. J.; Pershan, P. S.; Magnussen, O. M.; Ocko, B. M.; Deutsch, M.; Berman, L. E. *Physical Review B* **1997**, *55*, 15874–15884.

(124) Rice, S. A.; Zhao, M. *Physical Review B* **1998**, *57*, 13501–13507.

(125) Vitos, L.; Ruban, A. V.; Skriver, H. L.; Kollár, J. *Surface Science* **1998**, *411*, 186–202.

(126) Boden, S.; Eckert, S.; Willers, B.; Gerbeth, G. *Metallurgical and Materials Transactions A* **2008**, *39*, 613–623.

(127) Boden, S.; Eckert, S.; Gerbeth, G. *Materials Letters* **2010**, *64*, 1340–1343.

(128) Garcia-Muelas, R.; Lopez, N. *Nature Communications* **2019**, *10*, 2041–1723.

8 Acknowledgments

I want to express my gratitude to Prof. H.-P. Steinrück for the opportunity to do my PhD work at the chair of physical chemistry 2, and for the supporting and well organized environment at the chair.

Furthermore I want to thank the head of the surface and *in situ* spectroscopy group PD Christian Papp for the good supervision, always taking the time to discuss ideas and review measured data, and his countless helpful revisions and suggestions.

Special gratitude deserves my family, parents, grandparents and sister, who enabled me to pursue my studies and my good friends Paul and Jan-Paul.

Beyond that, I want to thank all the members and coworkers at the chair of physical chemistry 2 for the welcoming work environment. Special gratitude deserve Mathias Grabau, Michael Moritz and Christoph Wichmann for the supportive collaboration, and Bernd Kress and H.-P. Bäumler for their friendly support in technical matters.

Last but not least, I want to thank all collaboration partners from different fields and groups. It was a pleasure and privilege to work with so many great people.

9 Appendix

9.1 Appendix A - Publication P1

Publication 1 Haiko Wittkämper, Sven Maisel, Mingjian Wu, Johannes Frisch, Regan G. Wilks, Mathias Grabau, Erdmann Spiecker, Marcus Bär, Andreas Görling, Hans-Peter Steinrück, and Christian Papp, Oxidation induced restructuring of Rh-Ga SCALMS model catalyst systems *The Journal of Chemical Physics* 153, 104702-12 (2020).

`https://doi.org/10.1063/5.0021647`

9.2 Appendix B - Publication P2

Publication 2 Haiko Wittkämper, Sven Maisel, Michael Moritz, Mathias Grabau, Andreas Görling, Hans-Peter Steinrück, and Christian Papp, Surface oxidation-induced restructuring of liquid Pd-Ga SCALMS model catalysts *Physical Chemistry Chemical Physics* 23, 16324-16333 (2021).

`https://doi.org/10.1039/D1CP02458B`

9.3 Appendix C - Publication P3

Publication 3 Haiko Wittkämper, Sven Maisel, Michael Moritz, Mathias Grabau, Andreas Görling, Hans-Peter Steinrück, Christian Papp, Temperature-dependent XPS studies on Ga-In alloys through the melting-point *Surface Science* 717, 122008 (2022).

`https://doi.org/10.1016/j.susc.2021.122008`

9.4 Appendix D - Publication P4

Publication 4 Haiko Wittkämper, Rainer Hock, Matthias Weißer, Johannes Dallmann, Carola S. Vogel, Narayanan Raman, Nicola Taccardi, Marco Haumann, Peter Wasserscheid, Tzung-En Hsieh, Sven Maisel, Michael Moritz, Christoph Wichmann, Johannes

Frisch, Mihaela Gorgoi, Regan G. Wilks, Marcus Bär, Mingjian Wu, Erdmann Spiecker, Andreas Görling, Tobias Unruh, Hans-Peter Steinrück and Christian Papp, Isolated Rh atoms in dehydrogenation catalysis *submitted*, (2022).

`https://doi.org/10.21203/rs.3.rs-1791609/v1` (preprint)

9.5 Appendix E - Publication P5

Publication 5 Narayanan Raman, Sven Maisel, Mathias Grabau, Nicola Taccardi, Jonas Debuschewitz, Moritz Wolf, Haiko Wittkämper, Tanja Bauer, Mingjian Wu, Marco Haumann, Christian Papp, Andreas Görling, Erdmann Spiecker, Jörg Libuda, Hans-Peter Steinrück, and Peter Wasserscheid, Highly Effective Propane Dehydrogenation Using Ga-Rh Supported Catalytically Active Liquid Metal Solutions *ACS Catalysis* 9, 9499-9507 (2019).

`https://doi.org/10.1021/acscatal.9b02459`

9.6 Appendix F - Publication P6

Publication 6 Chantal Hohner, Miroslav Kettner, Corinna Stumm, Dominik Blaumeiser, Haiko Wittkämper, Mathias Grabau, Matthias Schwarz, Christian Schuschke, Yaroslava Lykhach, Christian Papp, Hans-Peter Steinrück, and Jörg Libuda, Pt-Ga Model SCALMS on Modified HOPG: Thermal Behavior and Stability in UHV and under Near-Ambient Conditions *The Journal of Physical Chemistry C* 124, 2562-2573 (2020).

`https://doi.org/10.1021/acs.jpcc.9b10944`